X-811-73-221

PREPRINT

NASA TM X-

PARABOLIC CYLINDER ANTENNAS

R. F. SCHMIDT

SEPTEMBER 1973

GSFC — GODDARD SPACE FLIGHT CENTER —

GREENBELT, MARYLAND

For information concerning availability
of this document contact:

Technical Information Division, Code 250
Goddard Space Flight Center
Greenbelt, Maryland 20771

(Telephone 301-982-4488)

X-811-73-221

PARABOLIC CYLINDER ANTENNAS

R. F. Schmidt

September 1973

GODDARD SPACE FLIGHT CENTER
GREENBELT, MARYLAND

PARABOLIC CYLINDER ANTENNAS

R. F. Schmidt
Network Engineering Division

ABSTRACT

This document discusses some of the features of single and dual parabolic-cylinder reflector antenna systems. It discusses these in terms of wave conversions, field divergence, and wavefronts in Fresnel and Fraunhofer regions. Beam-squinting by mechanical displacement and electrical phase gradient methods is introduced together with the combination of these methods. In the case of dual parabolic cylinders there is also a discussion of surface-truncation, parametric representation of surface intersections, main-aperture blockage by the subsystem, and beam squinting.

A few diffraction patterns are presented to illustrate the type of data available via a formulation equivalent to the complex-vector Kirchhoff-Kottler formulation. Main and cross-polarization components of the solution are available as they are inherently part of the field solution in the Cartesian coordinate system. A means of displaying main and cross-polarization components for arbitrary beam-scanning in (θ, ϕ) space is outlined. Extensions to monopulse tracking with variable-beamwidth (zooming) capability are introduced.

Page intentionally left blank

CONTENTS

ILLUSTRATIONS

ILLUSTRATIONS – continued

PARABOLIC CYLINDER ANTENNAS

INTRODUCTION

This report is applications-oriented and is fundamentally an extension of parabolic cylinder computations done on the undistorted gores of ATS-F[1]. The work was undertaken, initially, to explore the possibility of utilizing a parabolic cylinder to achieve multibeam capability in space for coverage of the continental United States, Alaska and Hawaii[2]. Cross-polarization characteristics are of prime interest in such a frequency re-use approach, as are antenna sidelobe levels. The same basic simulation technique used on ATS-F was employed here. Complex-vector Kirchhoff diffraction theory was applied to the problems and numerical integration was accomplished on the IBM 360/91 System at Goddard Space Flight Center.

Beam-squinting was studied for those cases where (1) line-feeds were displaced mechanically, anticipating a beam-switching arrangement, (2) phase gradients were imposed on each line-feed, and (3) a combination of the preceding two methods was employed. It was found that the general case of beam squinting created presentation difficulties since the basis vectors of the spherical coordinate system do not in general lend themselves to a convenient resolution of the antenna fields for a radiation pattern cut through the scanned beam maximum. Techniques were evolved to remedy this situation, but were not implemented in time for the present study. A verification of the approach was obtained later in extensive Nimbus G/EOS radiometer design evaluations. The subject data presentation scheme improved the means of displaying earth "foot print" patterns or contours and was related to beam synthesis, which is beyond the scope of this document.

In the course of the parabolic cylinder program development for the U. S. Multibeam Project an extension to dual parabolic cylinder geometry[3] was achieved. This entailed a redundant application of the basic mathematics and subroutines for parabolic cylinder antennas. Intermediate near-field integration was provided for the subsystem. Several unique features are associated with the dual parabolic cylinder approach, including the (ray-optics) conversion of waves from spherical to cylindrical to plane waves in the transmit mode. Line feeds are coalesced to directive point-source feeds, a significant simplification where a large number of independent antenna beams is required. Introduction

[1] Ref. 1

[2] Ref. 2

[3] Ref. 3, p. 10-11; Ref. 4, p. 116; Ref. 5; Ref. 6, pp. 335-339.

of the dual parabolic cylinder configuration also presented additional problems. The mathematical truncation (sometimes intersection) of surfaces was required, a serious obscuration of the main reflector by the subreflector had to be circumvented, and the means for achieving squinted beams was needed. For all of the preceding, actual calculations for a specific geometry and frequency of operation should be made to determine side lobe levels and cross-polarization characteristics. In passing, it is noted that the dual parabolic cylinder configuration affords several degrees of freedom for designing variable beamwidth (zoom) designs to aid in target acquisition and is inherently capable of preserving the complex-vector sum-and-difference beam characteristics associated with amplitude-sensing monopulse when zoomed.

SINGLE PARABOLIC CYLINDER ANTENNAS

The single parabolic cylinder antenna studied here was excited by means of a simple line-feed which was variously displaced in a parallel sense, and on which electrical phase gradients were imposed to achieve beam scanning. A basic difference between the ATS-F paneled-structure calculations[1] and those done here is the method of excitation of the reflector. In the former instance a directive point source, or at most a monopulse feed cluster, was used. In the present case an extended source (line-feed) was employed. Since it was not a priori known what dimensions, frequency, focal length etc. would ultimately be read into the problem, provision was made to superimpose the excitation from every element of the line source at an arbitrary point of the parabolic cylinder. In short, it was assumed that any point on the reflector surface might lie in the intermediate near-field or Fresnel region of the extended prime source of radiation. The details pertaining to the calculation of differential area, surface normals, polarization vectors, and superposition in the near field are well-know and will not be repeated here. Likewise, the proof that the Kirchoff-Kottler theory, and its equivalent representations, lead to Maxwellian fields will not be labored[2]. A number of these topics are discussed in detail in the section on dual parabolic cylinders in this report, therefore the results of the diffraction program for single reflectors are presented first and analytical considerations are deferred.

A candidate geometry for the U.S. MNBS Project is given below. These parameters were supplied as input to the parabolic cylinder subroutine together with the operating frequency, 12.0 GHz. The integration "stability" with respect to sampling of the illumination distribution was verified as a matter of routine

---

[1] Ref. 1

[2] Refs. 7,8,9,10

and found to lie close to 0.5 in both Cartesian coordinate directions[1]. Dipole sources were employed, therefore no input polarization moment was required beyond the field expression for the dipole itself[2]. A linear array of 98 dipole sources, each producing a field of the form

$$E_\theta = j\left(\frac{k}{\epsilon}\right)^{1/2} \frac{I_0}{2\pi R} e^{-jkR} \left[\frac{\cos\left(\frac{\pi}{2}\cos\theta\right)}{\sin\theta}\right]$$

was considered. All conversions between spherical, cylindrical, and Cartesian coordinates are performed within the program, as are translations of source phase centers. Angle conventions are made consistent, and dipole orientation is achieved via three Euler angles (α, β, γ).

$x_{min} = -3.00$ ft. $\quad x_{max} = 3.00$ ft.

$y_{min} = -2.00$ ft. $\quad y_{max} = 2.00$ ft.

$F = 2.28$ ft. $\quad z_1 = -F$

$f = 12.0$ GHz $\quad \lambda = 0.08196$ ft.

$LI_x = LI_y = 0.50$

$i = 98$

$\alpha = 90°$, $\beta = 90°$, $\quad \gamma = 0.0°$

---

[1] Spurious "grating-lobe" formation is obviously dependent on the sampling net utilized, and is far less likely to occur for geometries exhibiting axial symmetry and a polar net. The Cartesian net was used here because it conformed to the reflector geometry.

[2] Ref. 11, p. 98.

$$z = \frac{x^2}{4F_c} + z_1 \Rightarrow \text{parabolic cylinder with bounds indicated for (x) and (y) directions.}$$

Figure 1 shows the main polarization component of the far-field radiation pattern for the single parabolic cylinder antenna described above for the $\phi = 0°$ cut and Fig. 2 shows the same component for the $\phi = 90°$ cut. It can be seen that resulting beamwidths for these patterns agree fairly well with approximation formulas such as

$$BW \approx \frac{60\lambda}{D_i}$$

and that the narrower beamwidth is associated with the larger aperture dimension. Although the ratio of diameters (D_x/D_y) is 1.5, it is noted that the half-power beamwidths are in the (inverse) ratio of 1.25. Several factors are operative here and lead to a departure from the approximation formulas. Dipole sources were assumed[1], and the arbitrary orientation $\alpha = \beta = 90°$, $\gamma = 0°$ was employed. The illumination distribution taper is therefore determined by the directivity of the 98 sources, but more importantly, by the superposition of the fields of those sources at every point of the parabolic cylinder. Phase stationarity dominates problems of this type since an idealized cylindrical wave (singly infinite) has been replaced by a finite linear array viewed in the near field. The degree to which a finite array approximates a vector of an idealized cylindrical wave with respect to range, the laws of divergence, and wave-front purity, is discussed in greater detail in the section on dual parabolic cylinders and wave conversion by surfaces. The preliminary results depicted by Fig. 1 and Fig. 2 are at least reasonable for the selected input parameters.

A further objective was to obtain beam scanning or squinting by means of feed displacement. In actual practice electronic switching between feeds would be employed rather than physical displacement of the latter. Functionally the simulation attained scanning via x_e displacements of the line feed. Figures 3 and 4 show results corresponding to focal-plane displacements of $0.045'(\lambda/2)$ and $0.090'(\lambda)$, respectively. The approximation formula for laterally displaced feeds in paraboloids,

$$\sin\theta_s = \frac{K\Delta}{F}$$

[1] These would not have been acceptable sources for US MNBS, but provide a convenient means of illuminating the parabolic cylinder and ensuring that the program is operative.

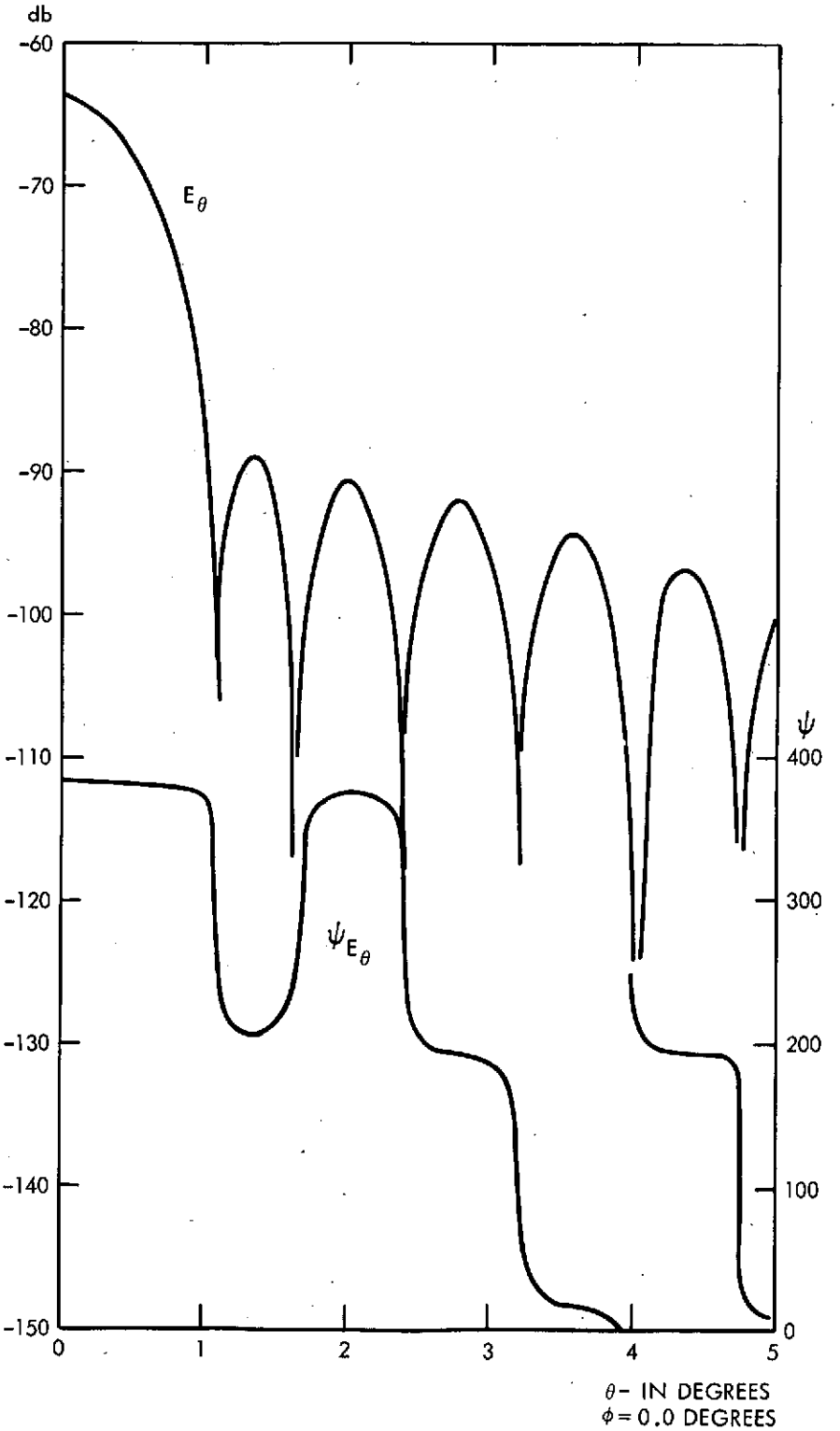

Figure 1. Fraunhofer pattern of single parabolic cylinder ($\phi = 0.0°$)

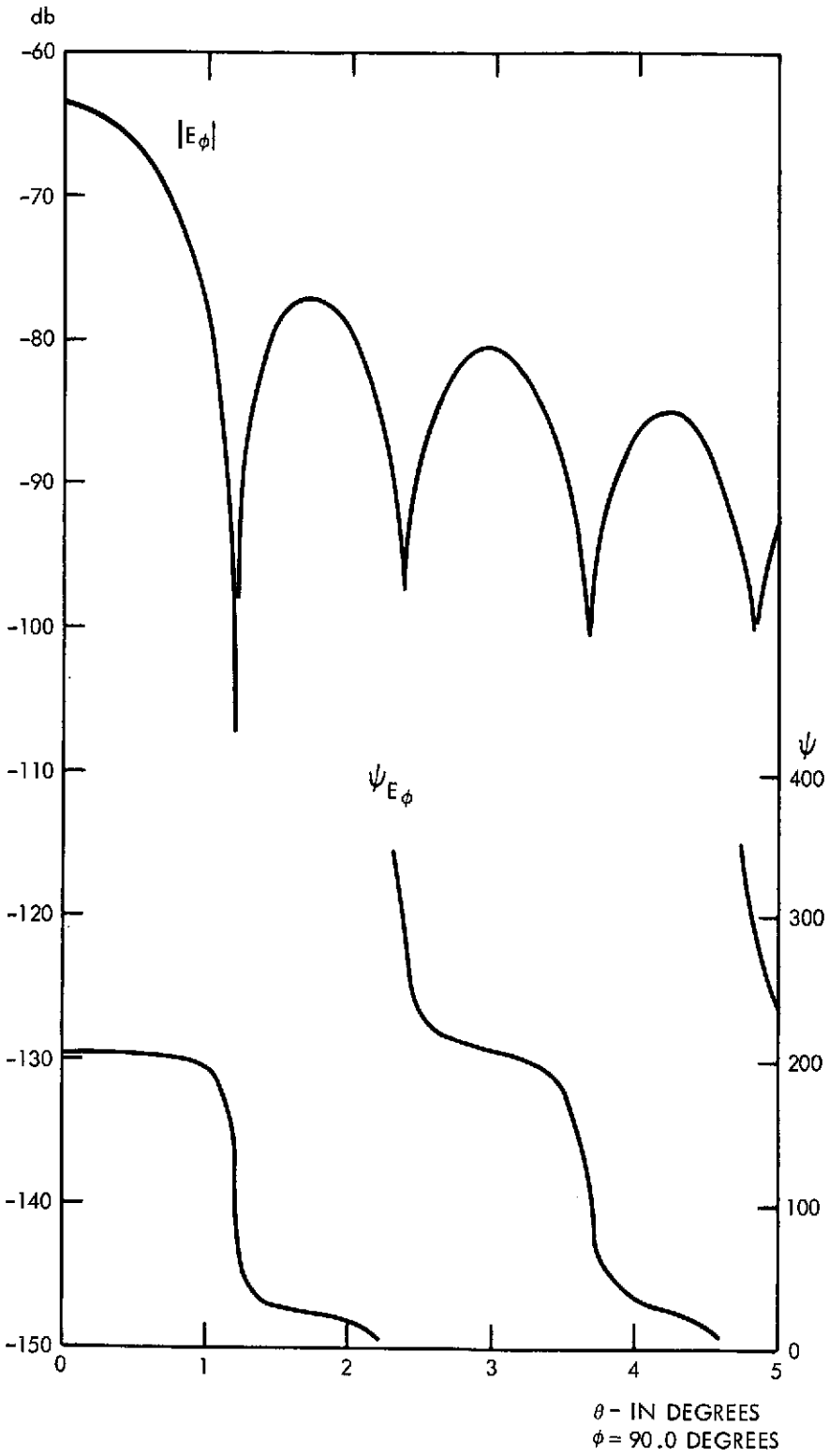

Figure 2. Fraunhofer pattern of single parabolic cylinder ($\phi = 90°$)

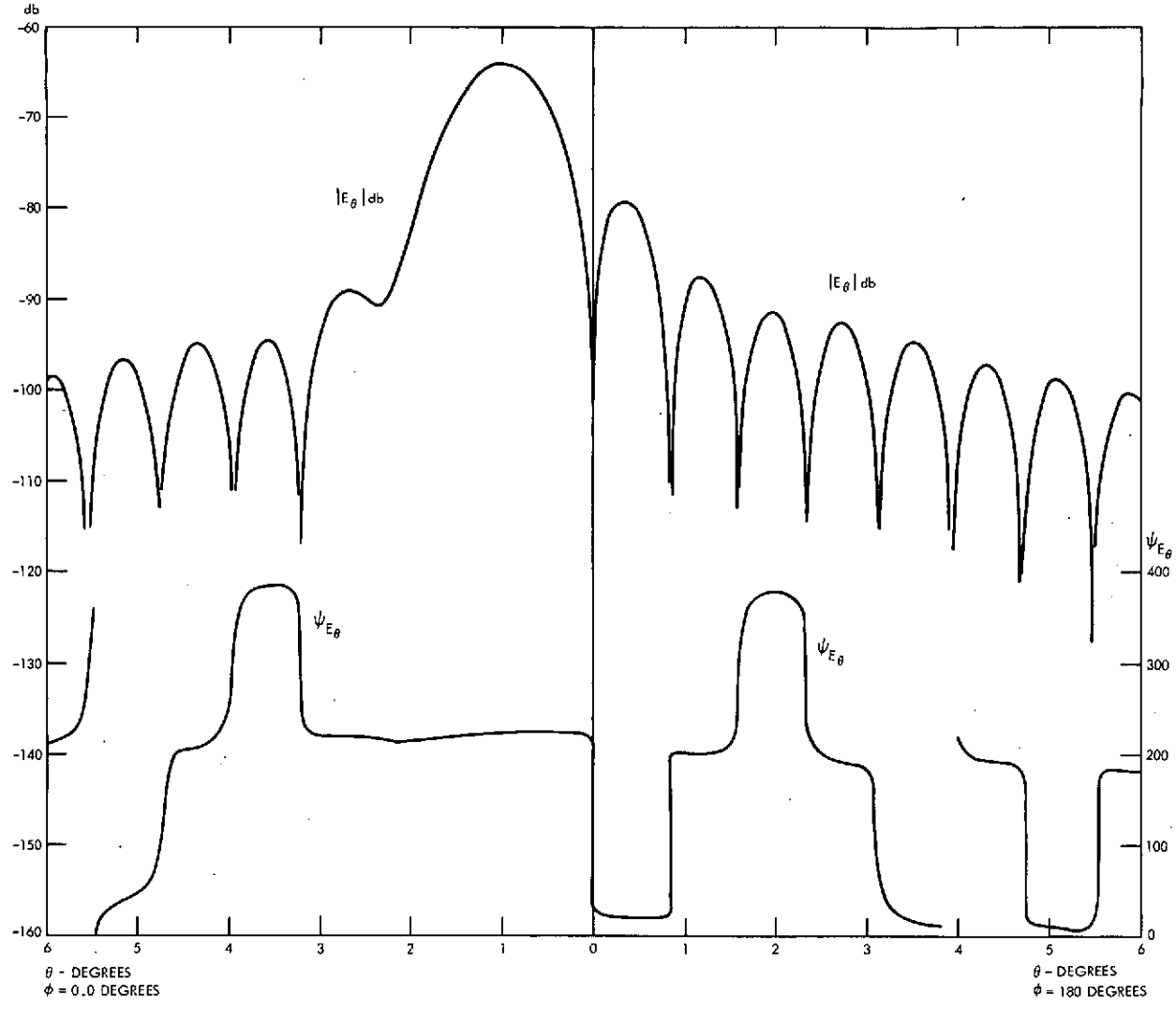

Figure 3. Squinted pattern for $x_\epsilon = \lambda/2$ ($\phi = 0°, 180°$)

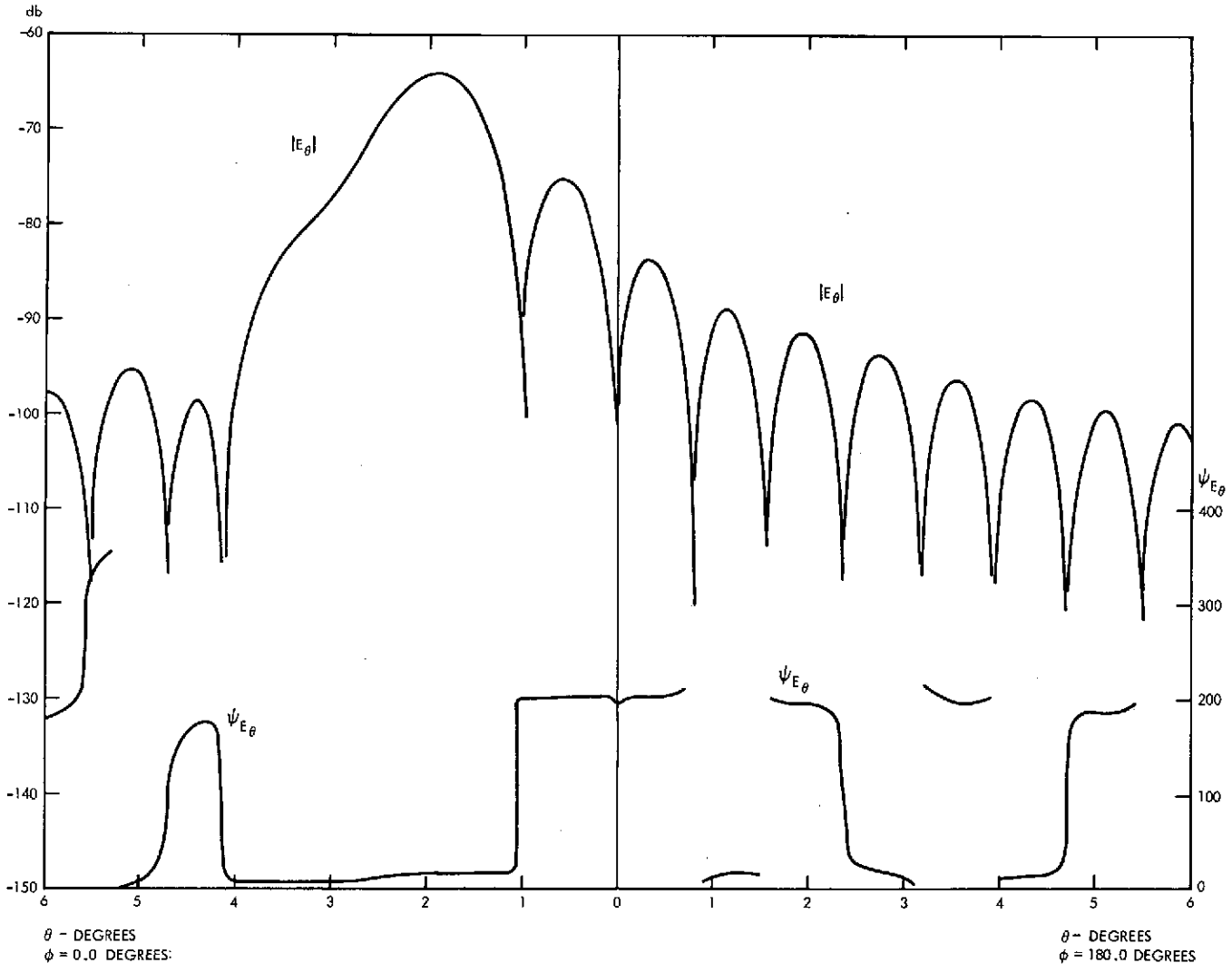

Figure 4. Squinted pattern for $x_\epsilon = \lambda$ ($\phi = 0°$, 180°)

yields squint angles of 0.99° and 1.98° whereas the simulation yields squint angles of 1.00° and 1.99° for the parabolic cylinder under study. The beam deviation factor K has a value of approximately 0.875 for the F/D_x of the present problem. Figures 3 and 4 demonstrate reasonable results from the simulation. Exhaustive studies to optimize side-lobe levels, gain, etc. were not carried out due to the termination of the multiple-beam antenna studies. Coma lobes of -15 db and -11 db were noted for these two cases of scan corresponding to approximately 1.25 BW(ϕ = 0°) and 3.50 BW(ϕ = 0°), respectively, for this rectangular aperture.

The next step in the development of the parabolic cylinder program was a verification of beam scanning, or squinting, by application of a linear phase gradient among the sources of the line-feed array. Figure 5 shows the result obtained for a gradient of 6.28 electrical degrees without line-feed displacement (i.e., $x_\epsilon \equiv 0$). The beam maximum is seen to appear at θ = 2.0°, ϕ = 90° with a coma-lobe level of about -12 db.

It is interesting to attempt to estimate the bearing angle at which the beam maximum emerges using array theory. Certainly one cannot apply the far-field array factors to the feed since every point on the parabolic cylinder is in the near-field region of the line-feed. Further, a squinted far-field beam from the array would not impose a phase gradient on the parabolic cylinder. If one tacitly assumes that the stationarity developed by the simulation using vector Kirchoff-Kottler theory is equivalent to that obtained by including an idealized cylindrical wave, then it can be argued that there exists an isomorphism between that wave and the aperture plane of the parabolic cylinder. Simple array theory can now be applied to the aperture plane distribution which carried the requisite phase gradient. One coalesces the rectangular distribution to a line distribution and utilizes the expression[1] for beam maximum location.

$$u_3 = \cos\theta = \left(h_3 - \frac{\alpha_3}{2\pi}\right)\frac{\lambda}{a_3}$$

It is convenient to set the line distribution that is actually along $\pm y$ to the $+z$ axis in order to obtain results easily. It is necessary to observe that the angle θ in the definition of u_3, above, differs from that of the diffraction simulation by $\pi/2$ radians or 90°. If the expression for u_3 is utilized, a scan angle of 88° results, which in the present set of conventions implies 2°, precisely the angle observed via the diffraction program. The diffraction program does

[1] See Ref. 12, page 27.

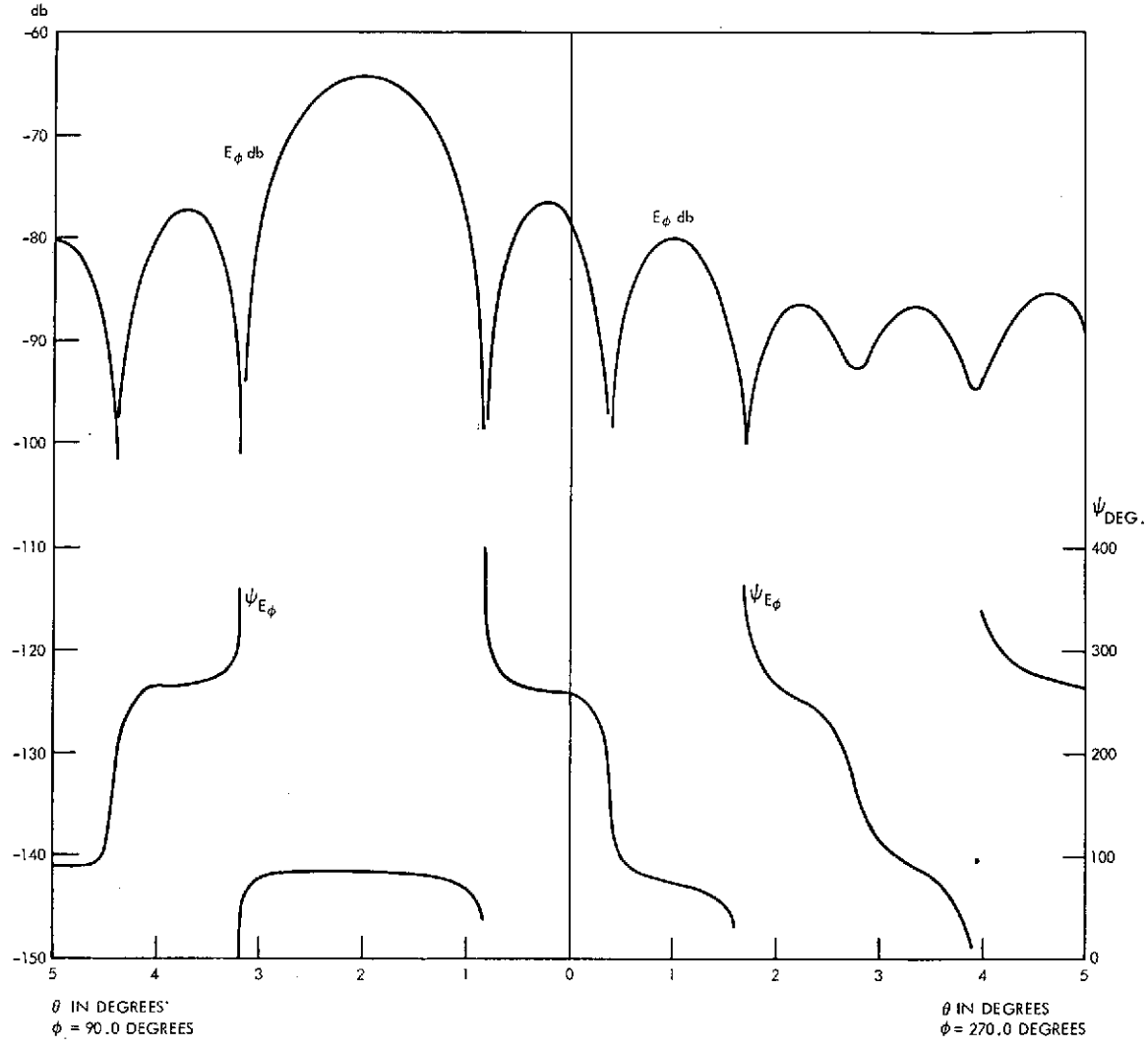

Figure 5. Squinted pattern for $\alpha = 6.28°$ gradient ($\phi = 90°, 270°$)

not, of course, utilize the preceding analogies, ray-optics concepts, etc. but proceeds along an entirely different computational route that entails a superposition of fields due to the 98 sources to obtain the total incident field. The incident field then interacts with the parabolic cylinder surface to produce electric sheet currents and charges. These quantities, in turn, are integrated under Kirchhoff theory to produce the backscattered far-field radiation pattern.

The combination of mechanical displacement, or switching, and phase gradient methods of achieving beam squint was tested and verified by simultaneously displacing the line feed in the amount $x_\epsilon = \lambda$ and applying the phase gradient $\alpha = 6.28°$ that had been used previously. Figure 6 shows the results obtained via the diffraction program. It should be noted that the Cartesian vector E_x is displayed rather than the polar components E_θ, E_ϕ. This is justified only when high-gain beams and small squint angles are being discussed. Since, for the present choice of input polarization,

$$E_x = (|E_\theta|^2 + |E_\phi|^2)^{1/2}$$

in the limit as $\theta \to 0°$. The main polarization component obviously cannot be described in terms of E_θ or E_θ alone when the beam maximum does not lie on the +Z axis. Figure 6 probably does not show the highest side-lobe level. The value $\theta = 2.75°$ at which the beam maximum is seen is a credible result considering the inputs. Each of the two factors influencing scan, x_ϵ and α, independently result in approximately 2° of beam displacement in orthogonal senses. One would, therefore, anticipate a total displacement angle $\theta \approx 2\sqrt{2}$ or about 2.8° in the $\varphi = 45°$ plane.

The preceding difficulties in presentation of the computed field led to the following technique which, although never implemented for the US MNBS program, has been utilized successfully on other projects. A new set of orthogonal output basis vectors is created in a manner entirely analogous to the method used to form incident electric and magnetic "polarization" vectors. The latter are easily developed via

$$\bar{c}_i = \frac{\bar{\rho}_1 \times (\bar{v}_i \times \bar{\rho}_1)}{|\bar{\rho}_1 \times (\bar{v}_i \times \bar{\rho}_1)|}$$

and

$$\bar{h}_i = \frac{\bar{\rho}_1 \times \bar{v}_i}{|\bar{\rho}_1 \times \bar{v}_i|}$$

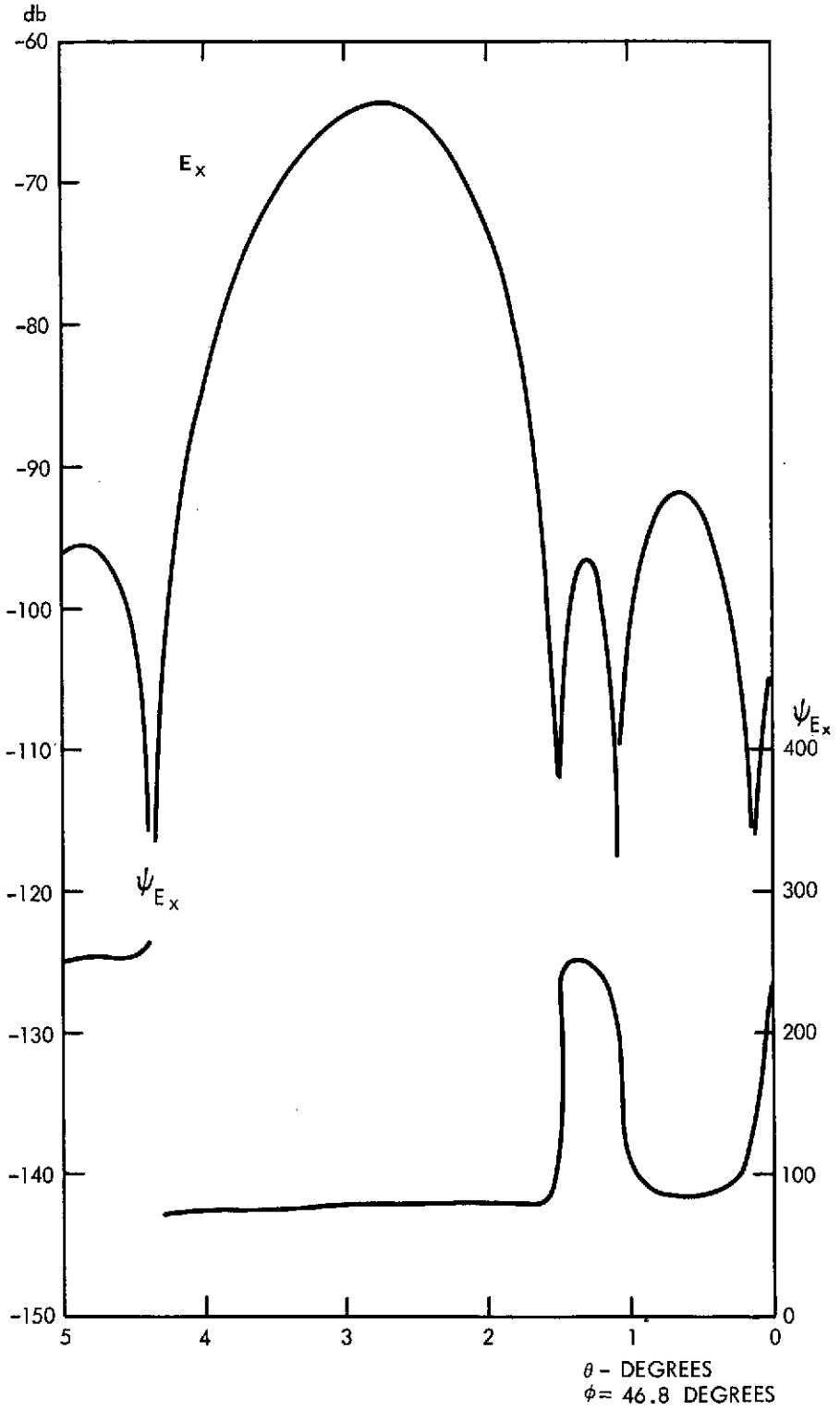

Figure 6. Squinted pattern for $x_\epsilon = \lambda$, $\alpha = 6.28°$ ($\phi = 46.8°$)

where $\bar{\rho}_1$ is a unit vector from radiation source to antenna surface, and $\bar{v}_i$ is the polarization moment. When polarization reciprocity exists it is convenient to create a pair of transverse orthogonal basis vectors

$$\bar{e}_1 = \frac{\bar{\rho}_{01} \times (\bar{v}_i \times \bar{\rho}_{01})}{|\bar{\rho}_{01} \times (\bar{v}_i \times \bar{\rho}_{01})|}$$

and

$$\bar{e}_2 = \frac{\bar{\rho}_{01} \times \bar{v}_i}{|\bar{\rho}_{01} \times \bar{v}_i|}$$

Here $\bar{\rho}_{01}$ is a unit vector from coordinate origin to far-field observer. It is then a simple matter to perform a dot product with the Cartesian total-field and the vectors $\bar{e}_1$ and $\bar{e}_2$ to provide a resolution into main-and cross-polarization components. Interestingly, representations of this type are also admirably suited to the computation of polarization efficiency when beam isolation is sought, between circular polarization states of opposite senses, for example[1,2].

DUAL PARABOLIC CYLINDER ANTENNAS

During the course of single parabolic cylinder investigation by means of the GSFC diffraction program the subject of dual parabolic cylinders arose. Apparently, in the context of LMSC, this referred to a redundant installation for the US MNBS project.[3] It is unclear whether or not LMSC contemplated the dual parabolic cylinder concept described in Reference 5 for this particular spacecraft application. The remainder of this report deals principally with that dual parabolic cylinder configuration which successively converts waves (under ray optics) from spherical to cylindrical to plane waves. In particular, the version of the antenna system which minimizes main reflector obscuration, as presented by Spencer, Holt, Johanson, and Sampson is considered. See Appendix A, which establishes the existence of a sector of a virtual cylindrical wave when a point source is used to illuminate a parabolic cylinder.

Although a 6' by 4' aperture operated at f = 12.0 GHz was specified for the US MNBS investigations and used in the single parabolic cylinder investigations,

[1] Ref. 13, p. 544

[2] Ref. 14, p. 183-187

[3] Ref. 2; p. 36, p. 45

subsequent basic computations for the "unexplored" dual parabolic cylinder configuration were done with various dimensions and frequencies to suit the convenience of the occasion, reduce turn-around time, and save cpu time on the computer. The "sugar-scoop" geometry shown in Fig. 7 evolves when cylindrical symmetry is exploited and the entire subsystem, including feed, is rotated to minimize main aperture obscuration. The dimensions used are no longer those associated with the original multibeam studies, and the frequency has been changed to 4.0 GHz. Arbitrarily, the focal-lengths of the parabolic cylinders were taken to be equal.

An interesting consequence of orienting the parabolic cylinders as shown in Fig. 7 is that the subreflector is now bounded at one end by the intersection ($\cap$) between the two surfaces (γ_1 and γ_2). A mathematical description of this intersection is required by the diffraction program to suitably restrict the integration under Kirchhoff theory. See Appendix B. Another interesting consequence of choosing this configuration is that near-field integration is now unavoidable since points on the main reflector lie in the near-field of the subreflector. See Appendix C. Last, but certainly not least for US MNBS, the question arises as to whether or not far-field beam scan or squint is possible in two orthogonal senses by displacement of the single point source that gives rise to a sector of a virtual cylindrical wave for this geometry. In other words, is it simultaneously possible to achieve minimum obscuration of γ_2 by γ_1 and retain a simple means to effect bidirectional beam swinging?

Before proceeding with the entire problem it may be well to consider the subsystem as a separate entity. From ray optics it is obvious that only a sector of a virtual cylindrical wave should be anticipated here. Under diffraction, for non-zero wavelength, one would expect an approximation to the sharp umbral-penumbral transitions across the geometrical bounds of ray-optics. The subsystem pattern which illuminates the main parabolic cylinder is obtained easily enough, but a suitable radial arc and line of observation needs to be chosen for, say, the subsystem of Fig. 7. Along this arc and line of observation the wave fronts should be identifiable if they conform to the virtual cylindrical wave. If a second, larger, radius of observation and the associated line are chosen, a second wavefront should be observed and the law of divergence of a cylindrical wave, with respect to wave intensity, should manifest itself. Since energy must be conserved, the electric (and magnetic) field should diverge as[1]

$$E_c \propto \frac{1}{\sqrt{r}} \ .$$

[1] Ref. 11, p. 76; Ref. 15, p. 339

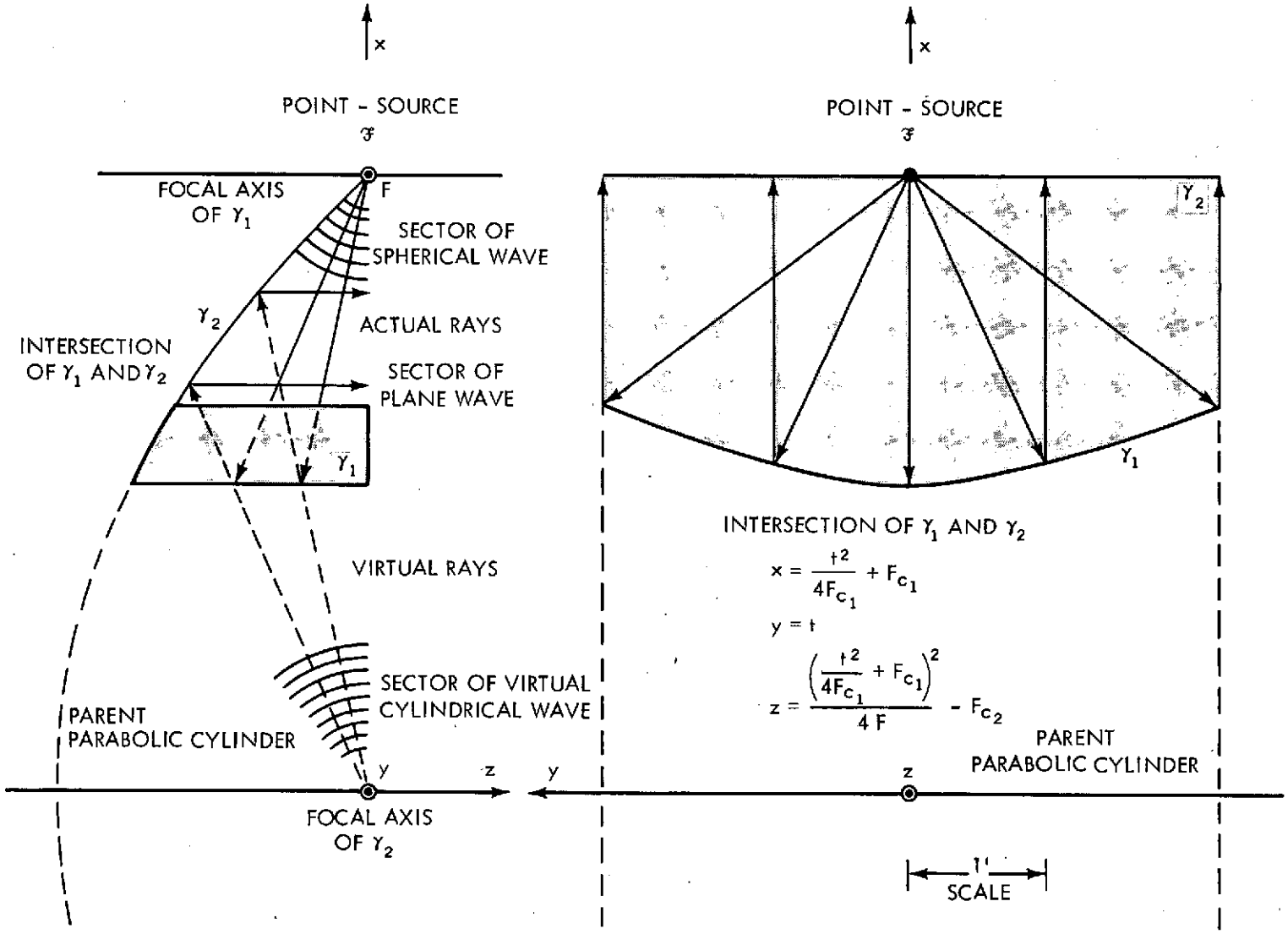

Figure 7. Dual parabolic-cylinder geometry

A series of diffraction calculations was done (at 8 GHz) for a subsystem very similar to the one for the "sugar scoop" design, however, the parabolic cylinder was symmetrically disposed with respect to the Z-axis. It was found that the virtual cylindrical wave behaved according to the spherical law of divergence

$$E_s \alpha \frac{1}{r}$$

at ranges in the vicinity of 25 to 100 miles, but did in fact satisfy the cylindrical law of divergence at 8F, 4F, 2F. It was also shown that a linear array with 98 dipole elements exhibited a divergence characteristic that was cylindrical in the near-field region and spherical in the far-field region. The latter result is generally accepted without question since the line array is commonly used to illuminate a parabolic cylinder. It is noted that the abstraction of a cylindrical wave is singly-infinite, but the sector of a cylindrical wave formed by either a point-source and parabolic cylinder or a linear array is, for all practical instances a finite wave with respect to directions parallel to the axis of symmetry of that wave sector.

The subsystem of Fig. 7 was probed subsequent to the limited basic studies of virtual cylindrical waves described above. Figure 8 shows a near-field line-probe field plot obtained via the diffraction program with the geometric bounds for the optically derived sector of a cylindrical wave indicated. It can be seen that the phase is nearly constant along the line of probing, within the geometric bounds, as it should be if a cylindrical wave exists. Also note the sharp cutoff of intensity across these bounds, amounting to about 4 db per wavelength for the first 10 wavelengths. The transition is a step discontinuity for ray-optics ($\lambda \equiv 0$). Figure 9 shows a near-field arc-probe field plot with the geometric bounds and the limit of visibility for the integration over the subreflector (γ_1). Again, it can be seen that the phase is constant to within ±15 electrical degrees here, within the geometric bounds, as it should be if a cylindrical wave exists. The cutoff of intensity is about 1 db per degree for the first 10 degrees. This transition would also be a step discontinuity for ray optics ($\lambda \equiv 0$). In conclusion, the subsystem diffraction patterns in the near field, along a line and an arc, demonstrate the existence of a virtual cylindrical wave over a sector bounded by geometric optics.

Since the subsystem behavior appeared satisfactory, the dual parabolic cylinder geometry was subsequently investigated and far-field radiation patterns were computed by means of the diffraction program. Figures 10 and 11 show the results for the $\phi = 0°, 180°$ and $\phi = 90°, 270°$ cuts. The latter are, of course,

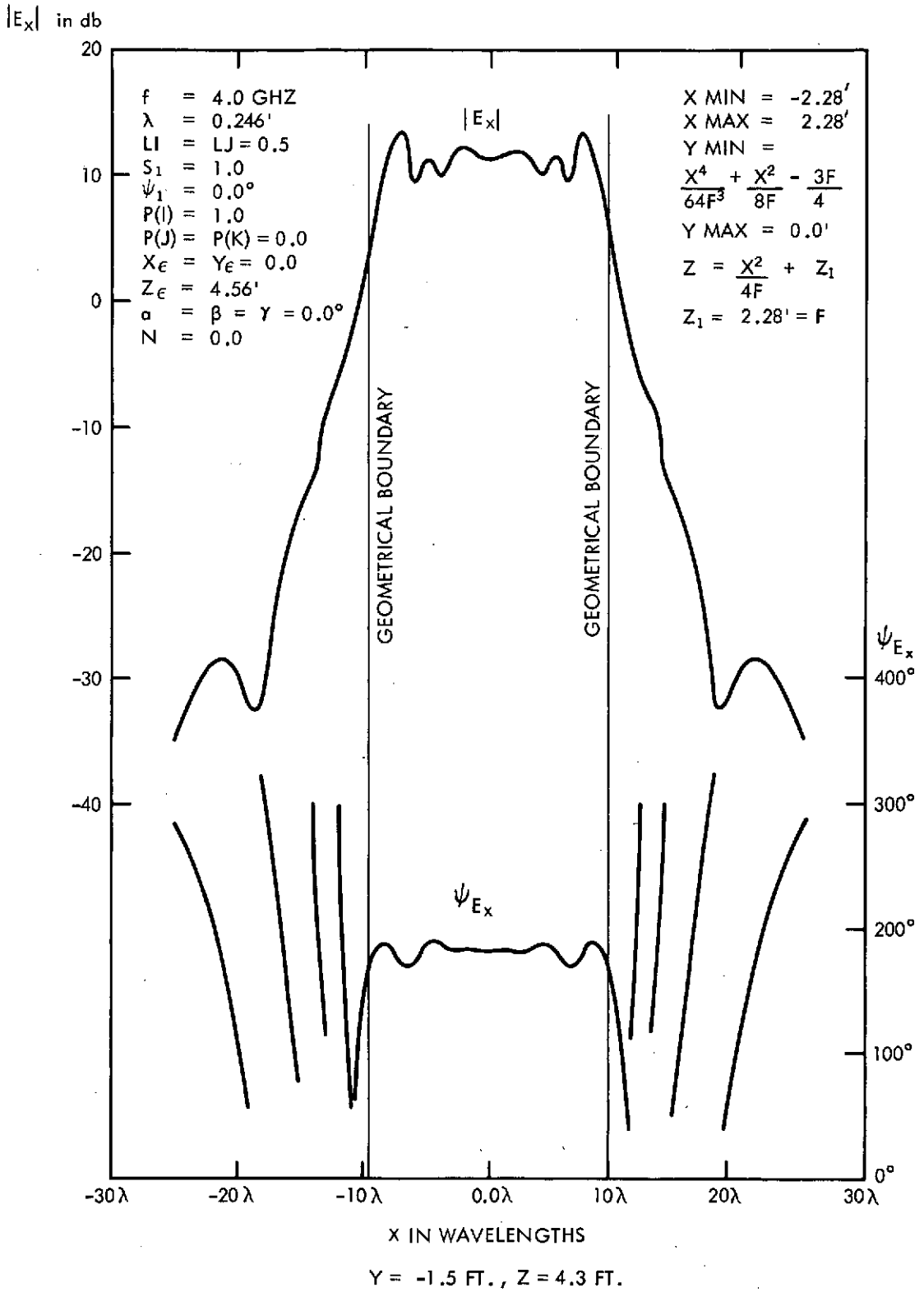

Figure 8. Fresnel pattern for subsystem (line locus)

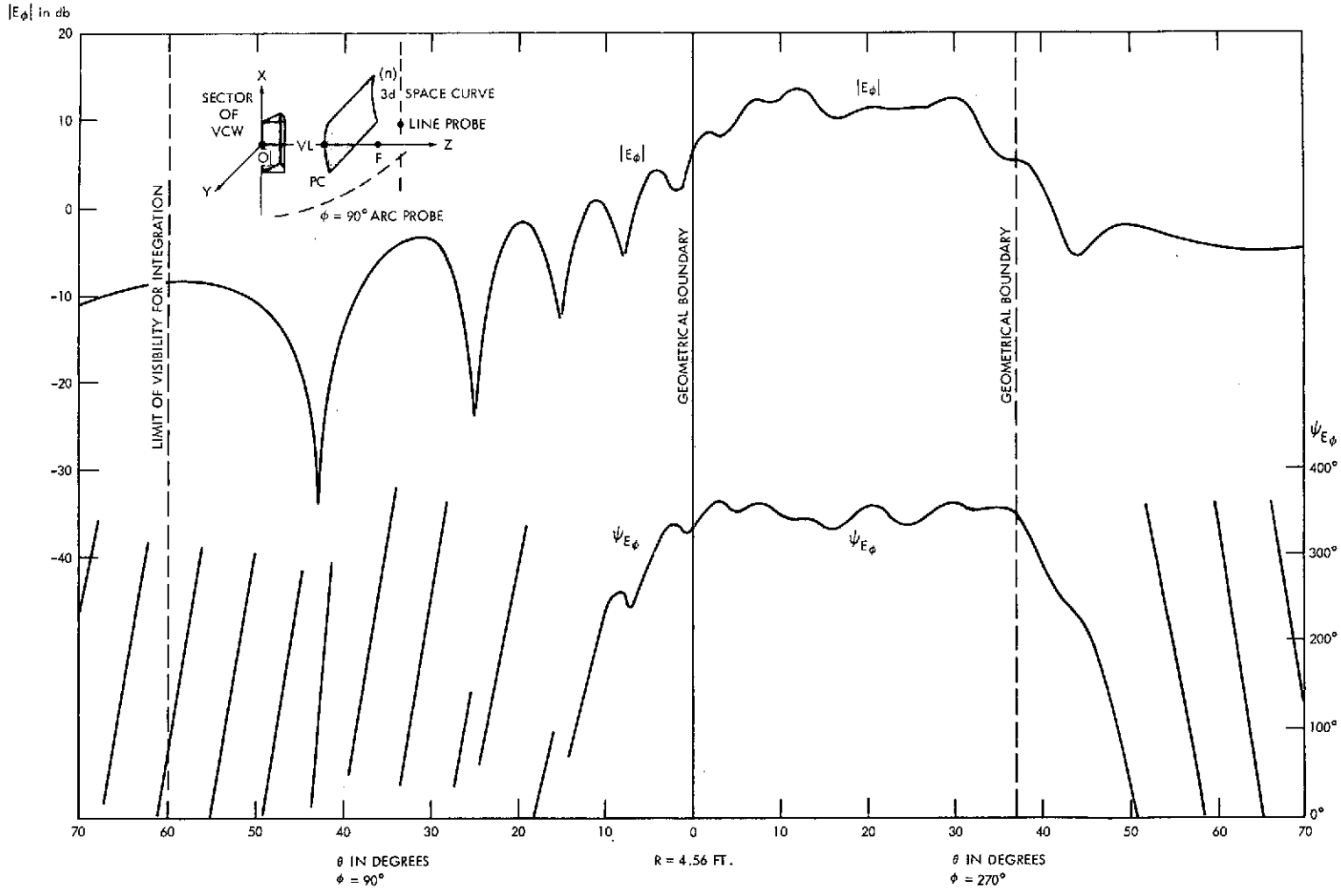

Figure 9. Fresnel pattern for subsystem (arc locus)

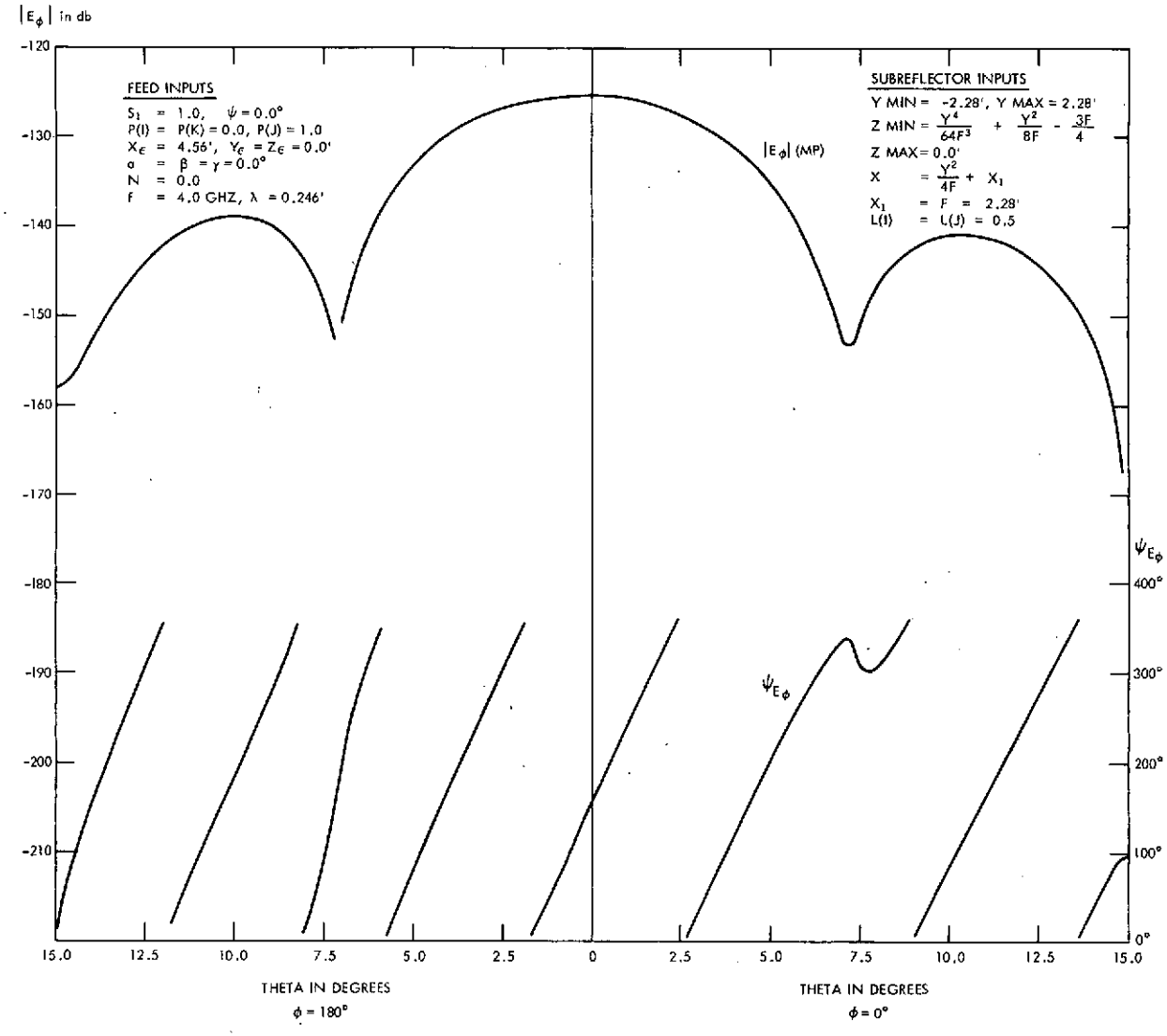

Figure 10. Fraunhofer pattern of dual parabolic cylinder system ($\phi = 0°, 180°$)

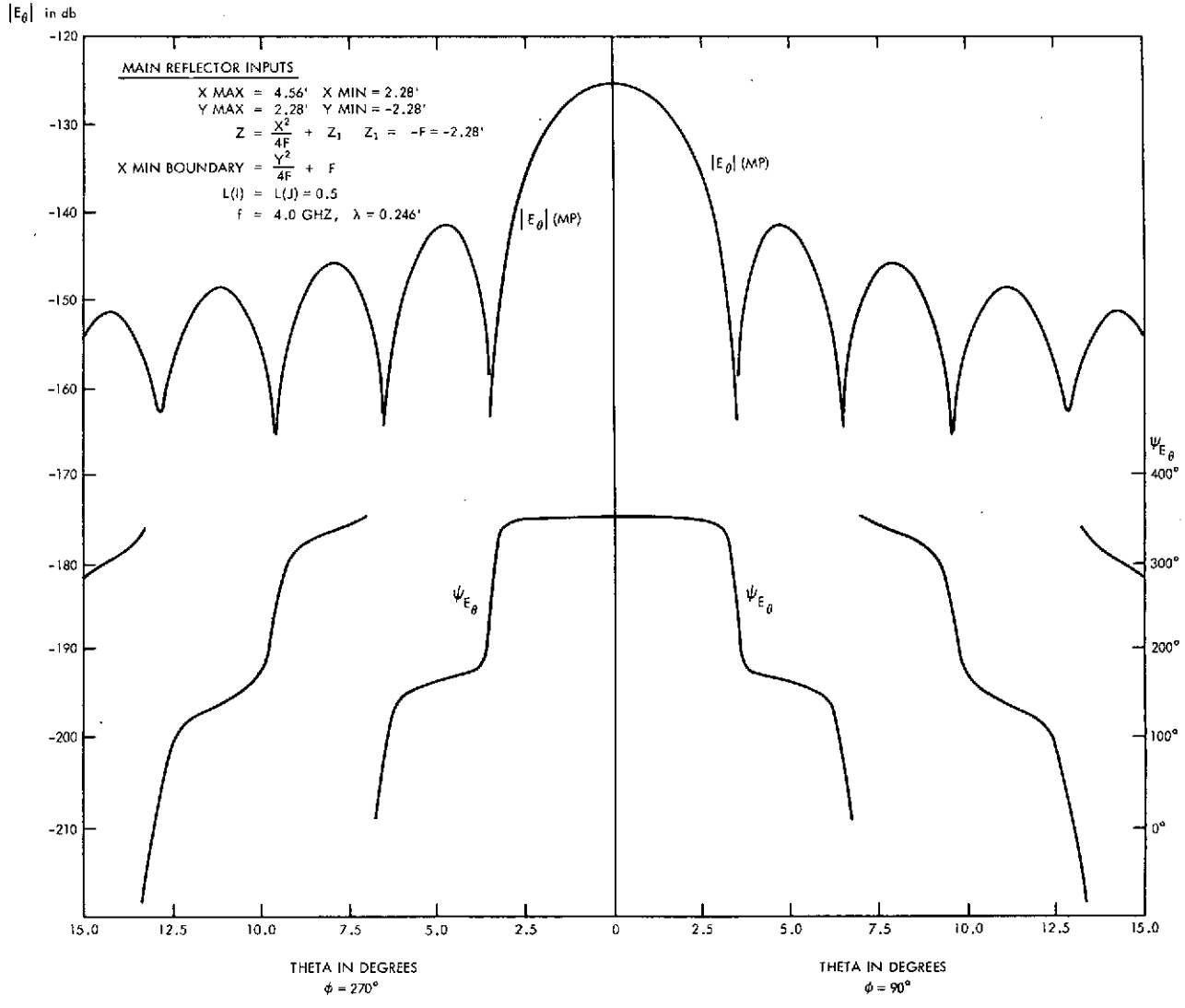

Figure 11. Fraunhofer pattern of dual parabolic cylinder system ($\phi = 90°, 270°$)

identical due to symmetry so only the $\phi = 90°$ cut was computed. No attempt was made for this limited study to attain side-lobe levels suitable to US MNBS and only first-principals were verified. An isotropic point source was employed ($N = 0$ in $E_i = \cos^N \Theta$).

Even with this prime illumination, modified slightly by differential space divergence to the edges of the subreflector, the side-lobe levels were about -15 db below the peak of the main beam. It is noted that the half-power beam-widths are reasonable for the dimensions of the main aperture at this frequency (4.0 GHz). Direct comparisons with approximation formulas for beamwidth are difficult since the lower edge of γ_2 is bounded by a 3-dimensional space curve ($\cap$), and illumination distribution on the main reflector is derived from a subsystem with planar symmetry only.

The non zero phase gradient of the far-field patterns of Fig. 10 is due to the fact that the bounding curve ($\cap$) for γ_1 and γ_2 produces an offset parabolic cylinder geometry with respect to the main reflector. The phase-center of the pattern from γ_2 lies about 3.5 feet above the center of rotation for the observer arc $\phi = 0°, 180°$. The phase gradient of the far-field patterns of Fig. 11 is essentially zero and should be, since the phase center of the pattern from γ_2 is not displaced with respect to the center of rotation for the observer arc $\phi = 90°, 270°$. The increasing gradient seen in Fig. 11 as θ increases is induced by the integration sampling criteria (LI = 0.5 here), and can be eliminated by refining the sampling net. In reality the gradients in the $\phi = 90°, 270°$ cut are identically zero and all phase discontinuities are π -radian jumps.

Since cross-polarization was of prime importance to US MNBS, some data illustrating cross-polarization are in order. Figure 12 shows the cross-polarized signal for the $\phi = 90°, 270°$ cut for the dual parabolic system being studied. The input polarization for the point-source was taken as $P(J) = 1.0$, a linear moment in the positive y direction. This moment was used to generate the polarization vectors by methods described earlier in this document. Cross-polarization data for the $\phi = 0°, 180°$ cut are not presented here since all values observed in the computation were at least 75 db below the level of the beam maximum.

All of the preceding computations for dual parablic cylinder antenna in this document can be considered preliminary inasmuch as the US MNBS effort was directed toward achieving a plurality of squinted beams. At this stage it is necessary to demonstrate that beam squinting in two orthogonal senses, separately and simultaneously, is possible. It will be recalled that line-feeds were coalesced to point-feeds at the expense of introducing a parabolic subreflector. This now precludes the utilization of the phase gradient method, demonstrated for single parabolic cylinders, to achieve beam squinting. It was

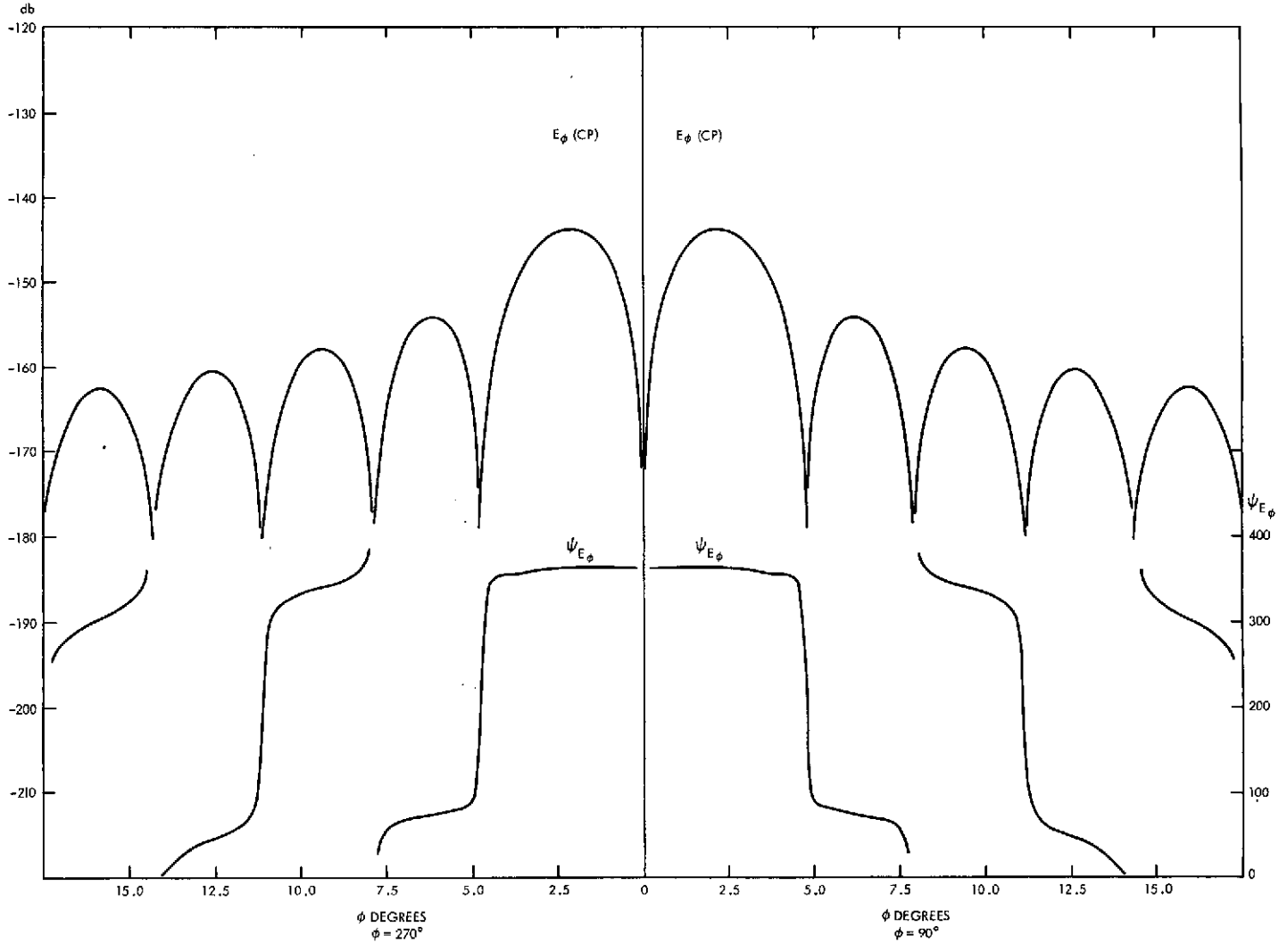

Figure 12. Fraunhofer pattern of cross-polarized field ($\phi = 90°, 270°$)

not entirely obvious what approach should be taken, and no guidelines had been discovered in the literature at the time this work was in progress.

Intuitively, the feed displacement approach in y_ϵ and z_ϵ directions for the geometry of Fig. 7, appeared to offer the degrees of freedom required. A ray-optics analysis for an offset feed would undoubtedly be very complicated, and ray-tracing would be tedious with only qualitative results likely to result, therefore, the GSFC diffraction program was used to explore the feed displacement approach. The confidence level in the program was high since subsystem fields and axial far-field patterns previously appeared satisfactory in all respects. A single vector, $\bar{\rho}_\epsilon$, is used to displace feeds, and constitutes an input (empty or otherwise) for every problem submitted to the computer. No program modifications were required to explore the possibility of beam-squinting by means of feed displacement for dual parabolic cylinder configurations.

The first attempt to squint the secondary radiation patterns was by means of a z_ϵ displacement of minus one wavelength. The second attempt was by means of a y_ϵ displacement of plus one wavelength. For each of these feed displacements the principal-plane cuts $\phi = 0°$, 180° and $\phi = 90°$, 270° were taken to verify independent orthogonal beam squinting. The third attempt was by means of simultaneous displacements $z_\epsilon = -\lambda/2$ and $y_\epsilon = +\lambda/2$, for which the $\phi \approx 300°$ cut contains the beam maximum since the antenna has, effectively, two unequal squinting factors.

Figures 13 and 14 show the squinted beams for z_ϵ and y_ϵ displacement, respectively. An isotropic source, N = 0, was employed since only the squinting phenomena was sought here, and not optimization of the system with respect to gain and side-lobe level. It can be seen that the beamwidth for the $\phi = 0°$, 180° cut is approximately 6.4° with a coma lobe of -12.3 db for a squint of 3.75°, which should be contrasted to a beamwidth of 6.1° with -15.0 db side lobes for the axially directed beam in the same angular cut. The beamwidth for the $\phi = 90°$, 270° cut is approximately 3.0° with a coma lobe of -12.4 db for a squint of 5.2°, which should be contrasted to a beamwidth of 2.8° with -16.0 db sidelobes for the axially directed beam in this angular cut.

Figures 15 and 16 are the companion cuts to Figs. 13 and 14. They simply verify that there is no anomalous behavior of the beams when squinting is being accomplished by displacing feeds in the minus z_ϵ and plus y_ϵ directions. It can be seen from Fig. 15 that, in the $\phi = 90°$, 270° cut, the z_ϵ displacement has not affected the beamwidth significantly, but side lobes have degraded from -16 db to about -13 db using N = 0 for the feed function. Similarly, it can be seen from Fig. 16 that, in the $\phi = 0°$, 180° cut, the y_ϵ displacement has only affected the beamwidth somewhat, an increase of about 20%, and side lobes have degraded from -15 db to about -11 db.

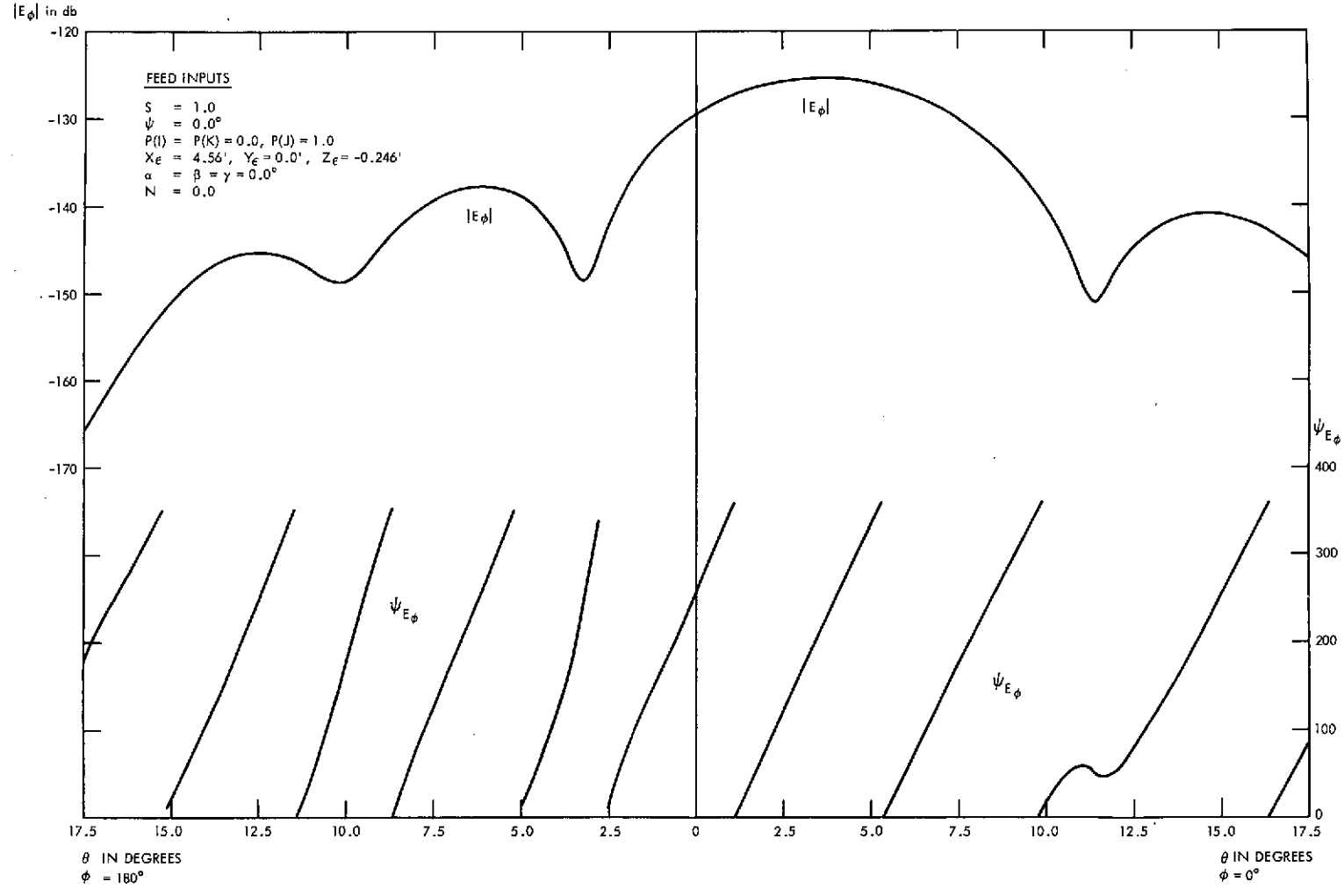

Figure 13. Squinted pattern for $z_\epsilon = -\lambda$ ($\phi = 0°$, 180°)

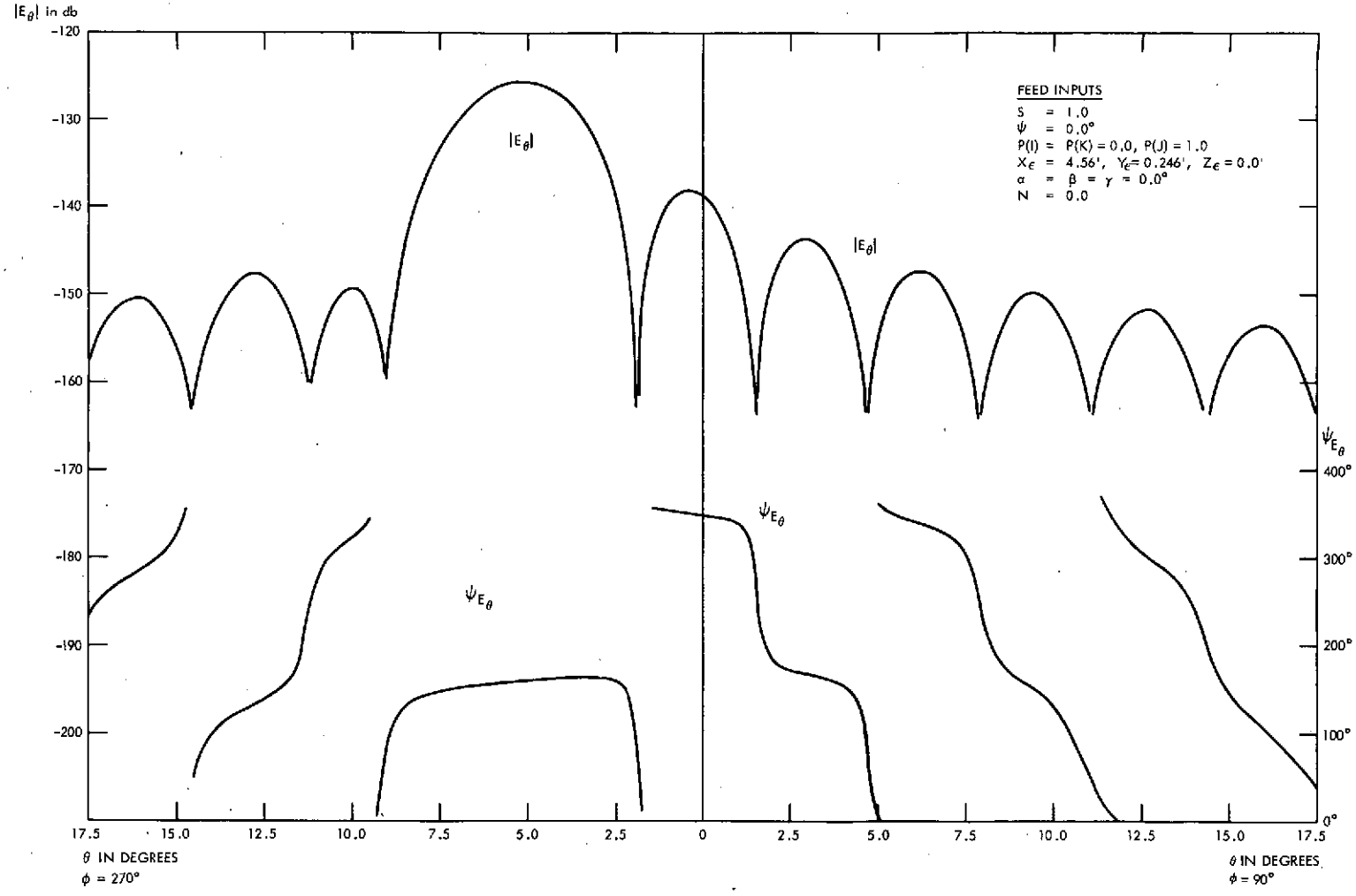

Figure 14. Squinted pattern for $y_\epsilon = +\lambda$ ($\phi = 90°, 270°$)

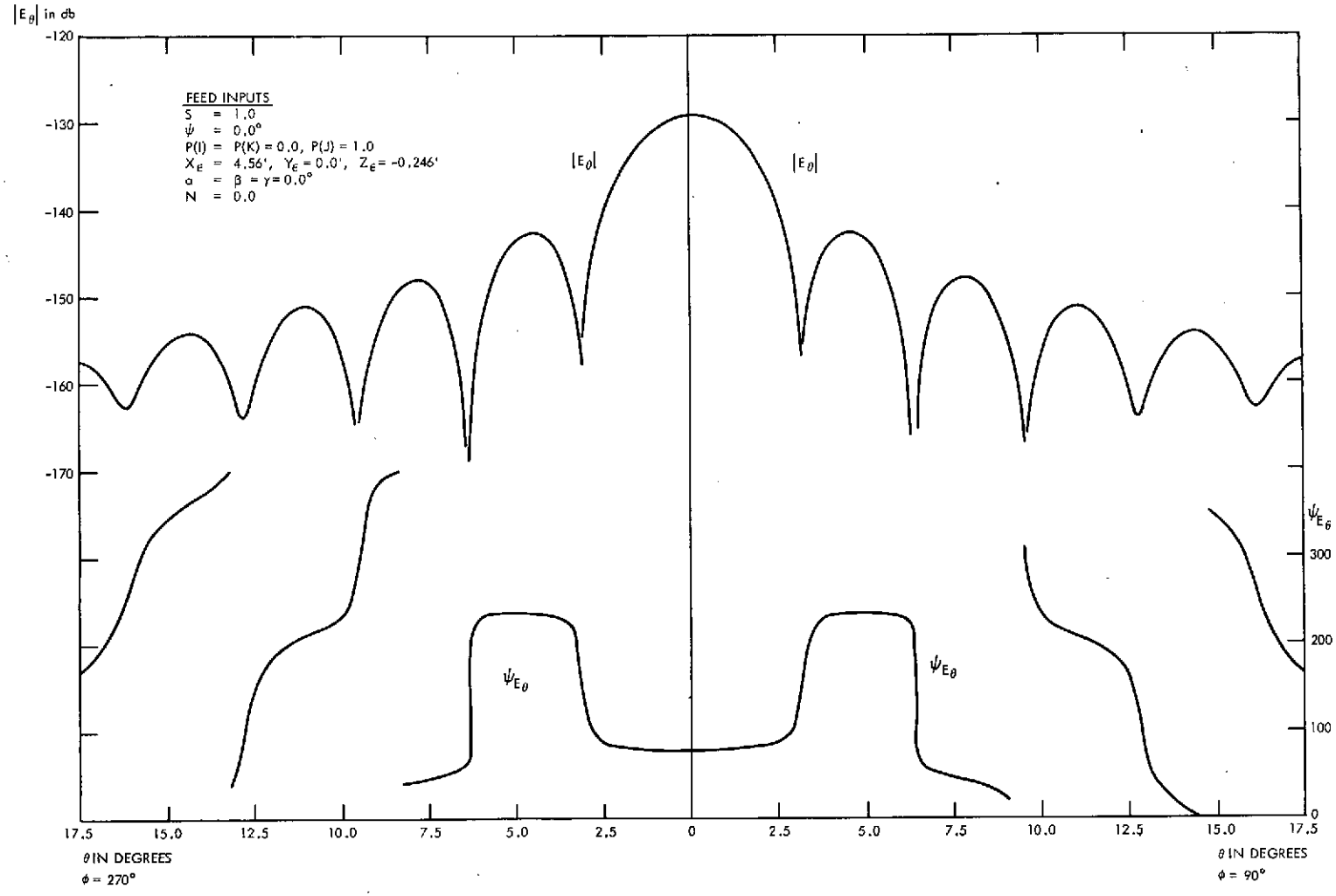

Figure 15. Squinted pattern for $Z_\epsilon = -\lambda$ ($\phi = 90°, 270°$)

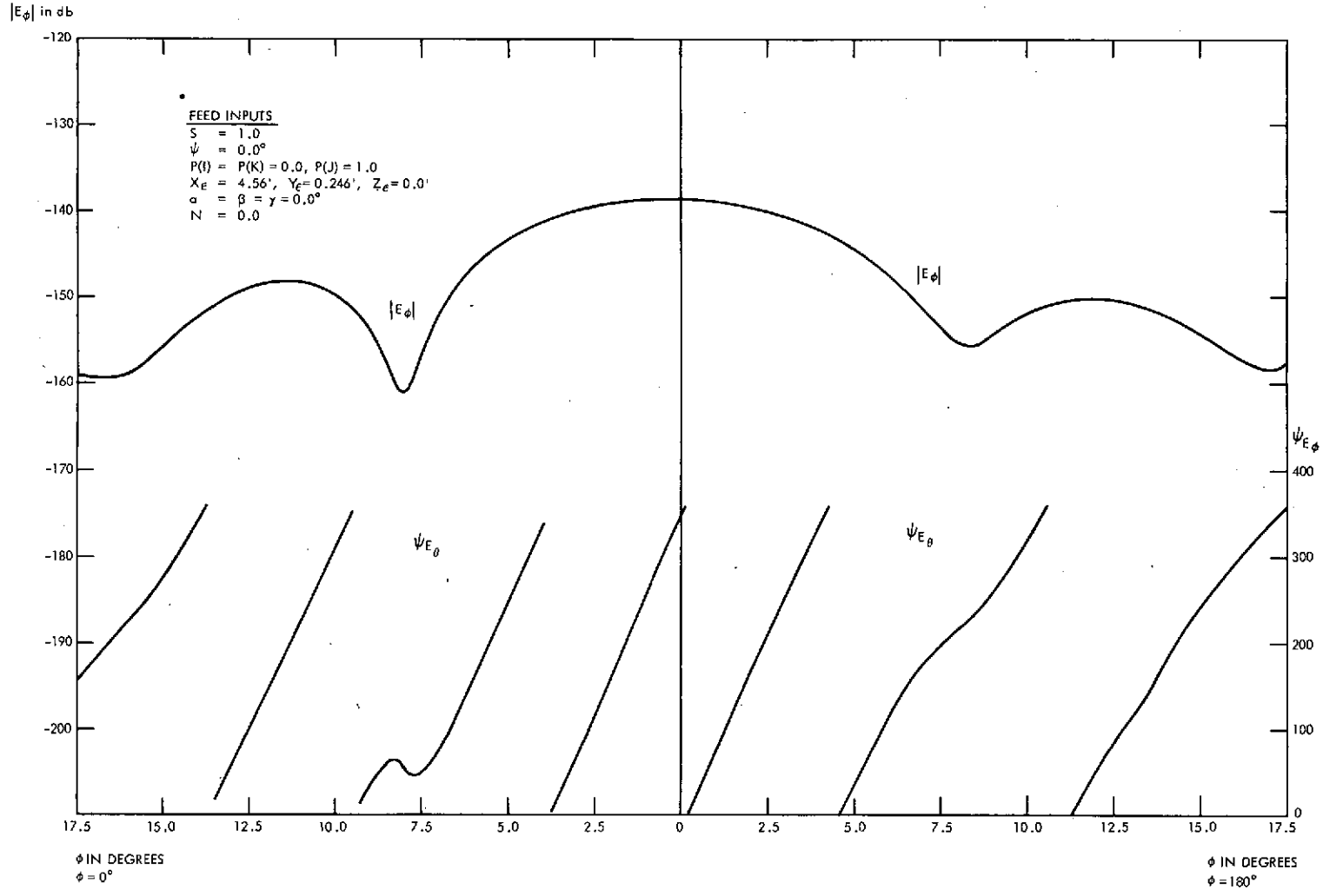

Figure 16. Squinted pattern for $Y_\epsilon = +\lambda$ ($\phi = 0°, 180°$)

Figure 17 shows the results of squinting the beam by simultaneous displacements of $z_\epsilon = -\lambda/2$ and $y_\epsilon = +\lambda/2$. The beam maximum was recovered in the $\phi = 120°, 300°$ cut. The Cartesian field E_y was plotted since the spherical basis vectors $\hat{i}_\theta$ and $\hat{i}_\phi$ at these values of ϕ do not lend themselves for an easy presentation of the total field as described previously. A coma lobe of -15 db level can be seen in Fig. 17, and the beamwidth is approximately 3.5°. It should be recalled that the present aperture yielded a beamwidth of 2.8° in the $\phi = 90°$, 270° cut and 6.1° in the $\phi = 0°$, 180° cut without any feed displacement, the case of zero squint. The observed beamwidth is therefore credible, and the side-lobe level of -15 db acceptable in view of the illumination employed. Figure 17 illustrates the possibility of obtaining squint in two orthogonal directions in varying degree, to achieve the type of capability needed for projects like US MNBS. Implicit, of course, is the capability of achieving amplitude-sensing monopulse from a cluster of four secondary beams which are squinted as in Fig. 17.

The US MNBS Program did not require monopulse capability, but only a plurality of squinted beams. Since results such as those of Fig. 17 demonstrated bidirectional beam squinting, the investigation of this dual parabolic cylinder geometry was prematurely considered "complete" for purposes of this report. It was noted, however, that the subject configuration shows promise for bidirectional continuously variable beamwidth control. In the course of investigating the "zooming" properties for this antenna, the subject of monopulse was introduced since considerable interest attaches to target acquisition by means of a variable beamwidth sum pattern and a variable error-channel slope. Initially some difficulty was encountered in producing good monopulse difference patterns. The problem was traced to the intuitive y_ϵ and z_ϵ displacement relied upon to produce the four squinted beams.

Either ray optics or diffraction theory suffice to clear up the matter. See Fig. 7. Under reception, the incoming rays from a plane wave directed along the negative Z-axis converge to a true point-focus (F) after interacting with both γ_2 and γ_1, in that order. Subsequently they diverge from F. If the central ray of a convergent or divergent ray bundle is assumed orthogonal to an Airy type distribution consisting of a bright disc and ring structure, then it should also follow that the wavefronts associated with the isophotes are orthogonal to this central ray. In short, the feed positions for satisfactory monopulse performance, and for simple beam-squinting as in US MNBS, should consider the orientation of the wavefronts in the focal region. For the case at hand, Fig. 7, $\pm y_\epsilon$ suffices for a first pair of feeds, with respect to the focal point, but $\pm z_\epsilon$ and $\mp x_\epsilon$ displacements are required for the second pair of feeds.

Six figures provide detailed data on the focal region fields. The geometry is that of Fig. 7, and zooming is introduced here. Fig. 18 illustrates electric field isophotes, Fig. 19 electric field wavefronts and Fig. 20 the time-average

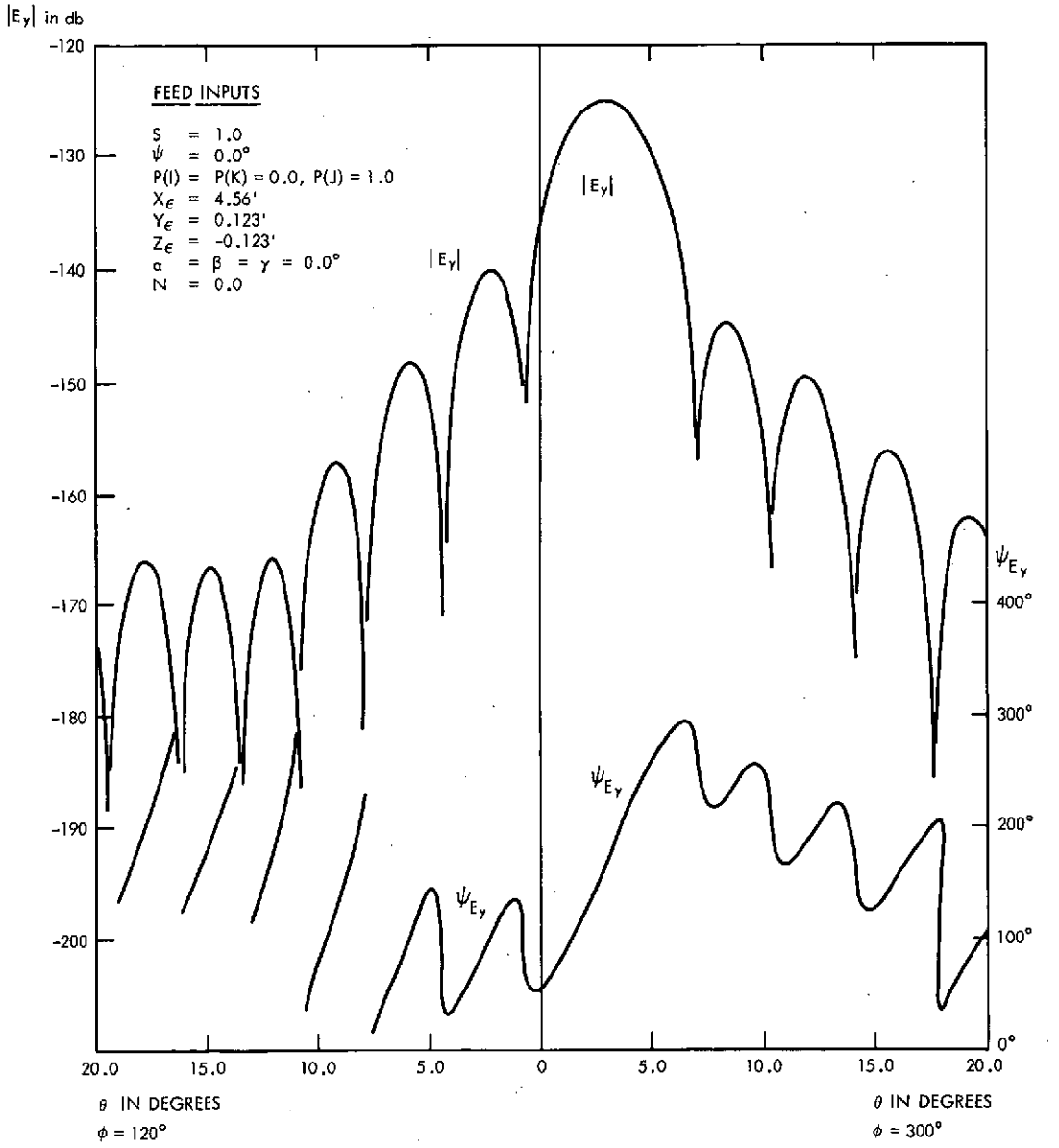

Figure 17. Squinted pattern for $Z_\epsilon = -\lambda_\epsilon$ $Y_\epsilon = +\lambda/2$ (ϕ = 120°, 300°)

Poynting vectors. The extreme or boundary rays from ray-optics are superimposed on all three plots to illustrate the differences and similarities between ray-optics and diffraction theory. It can be seen that the Airy bright ring structure is inclined with respect to the central ray, which differs markedly from the ring structure of a paraboloid receiving an axially directed plane wave. The depth of field (to the nulls or zero intensity isophote) along the central ray is poorly defined compared to a paraboloid. Zero field values are associated with phase singularities since there is no rational definition of phase at these points. The width of field is well-defined. A phase velocity of about 1.1 that of free space is noted in the focal region. In addition, regions of energy counterflow can be identified in the Poynting vector plots, but cannot be inferred from the isophote or wavefront information alone.

Analogies to hydraulics can be made here. When a (null) limit of the depth of field is distinct it corresponds to a virtual obstacle in the path of the main energy flow. Other null fields are associated with a vortex or stagnation point. The phenomena of increased phase velocity has its counterpart in uniform flow with a constraint (Bernoulli's law for the product of velocity times area) and is found in the transition from a converging spherical wave, to a plane wave, to a diverging spherical wave in vicinity of the focus (F).

The focal-region data of Figs. 21-23 are similar to those of Figs. 18-20 except that the non-intersecting portion of the subreflector has been telescoped mechanically to achieve zooming. As a result the Airy disc and bright-ring structure has been broadened and the inclination has changed. An application of ray-optics provides a rapid, if qualitative, appreciation of the consequences of zooming. Obviously the two ends of the main reflector can also be telescoped mechanically to achieve zooming in the orthogonal sense, but this will not result in a differential inclination of the Airy disc. This case is not illustrated here, but it is noted that diamond monopulse is a logical choice for the dual parabolic-cylinder zoom antenna since only two feeds are then required for each error channel. One pair of feeds must be rotated in synchronism with the telescoping of the subreflector effecting the zooming. The other pair of feeds need not be rotated to achieve monopulse operation unless their source patterns are highly directive.

SUMMARY

A computer program has been developed which is suitable for studying the performance of single and dual parabolic cylinder antennas with regard to feed design, near-field effects, cross-polarization effects, side-lobe level, and directive gain. It has been shown that line feeds associated with single parabolic cylinder configurations can be coalesced to point feeds by introducing the dual parabolic cylinder concept to attain a multibeam capability. A geometry which

X IN WAVELENGTHS
23
22
21
20
19
18
17
16
15
14
-5.00
-4.00
-3.00
-2.00
-1.00
0.00
1.00
2.00
3.00
4.00
5.00
Z IN WAVELENGTHS

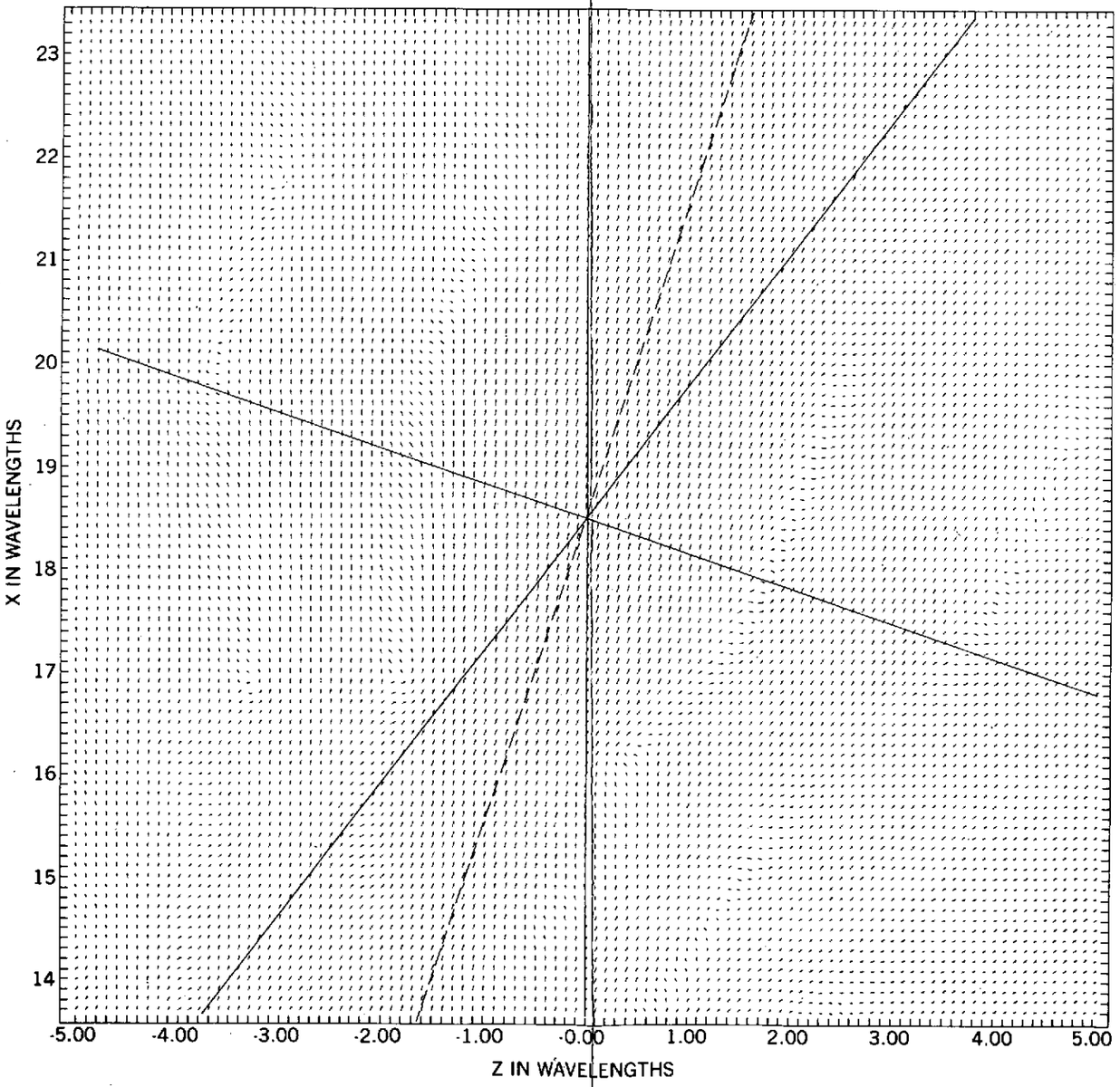

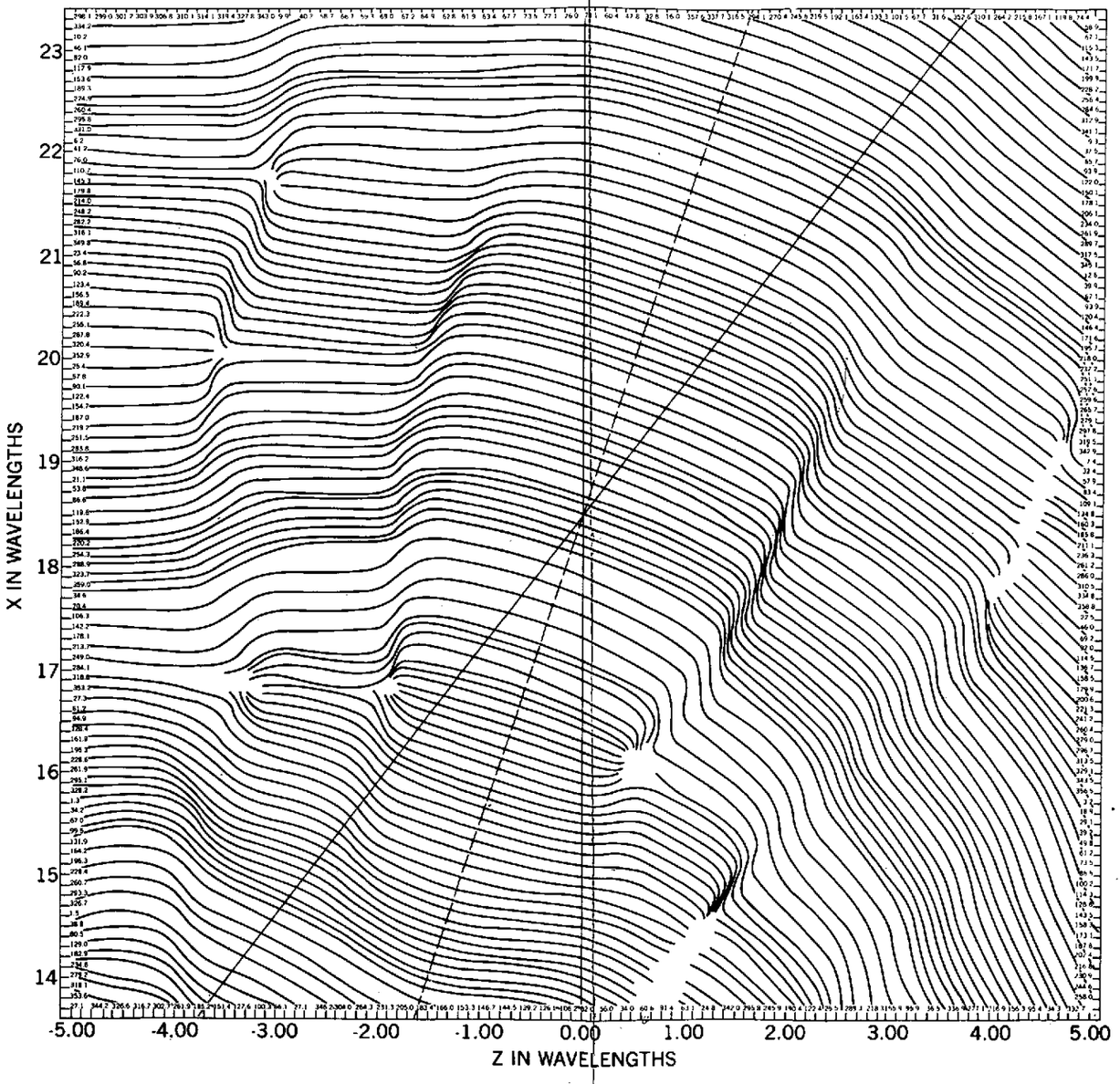

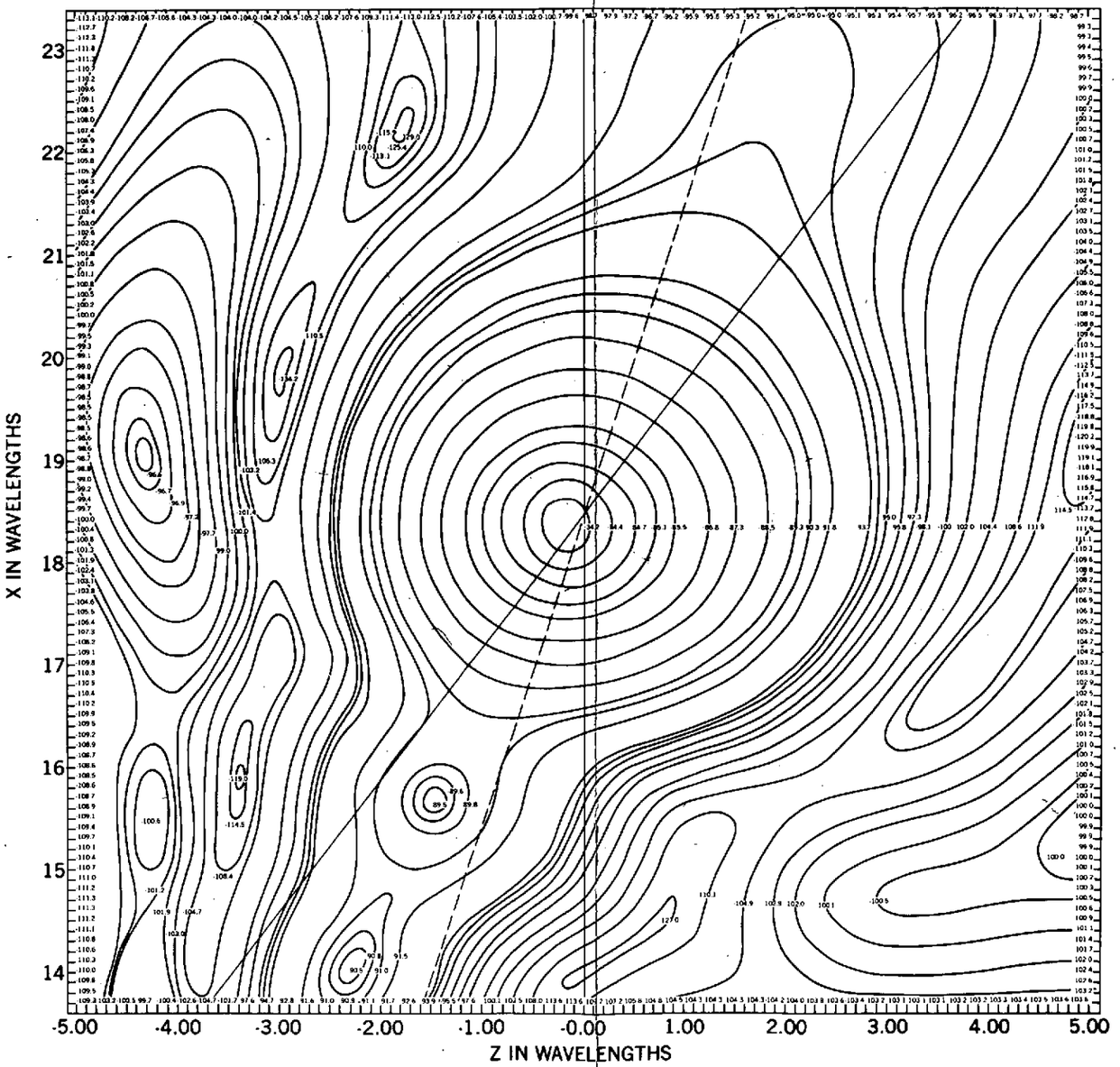

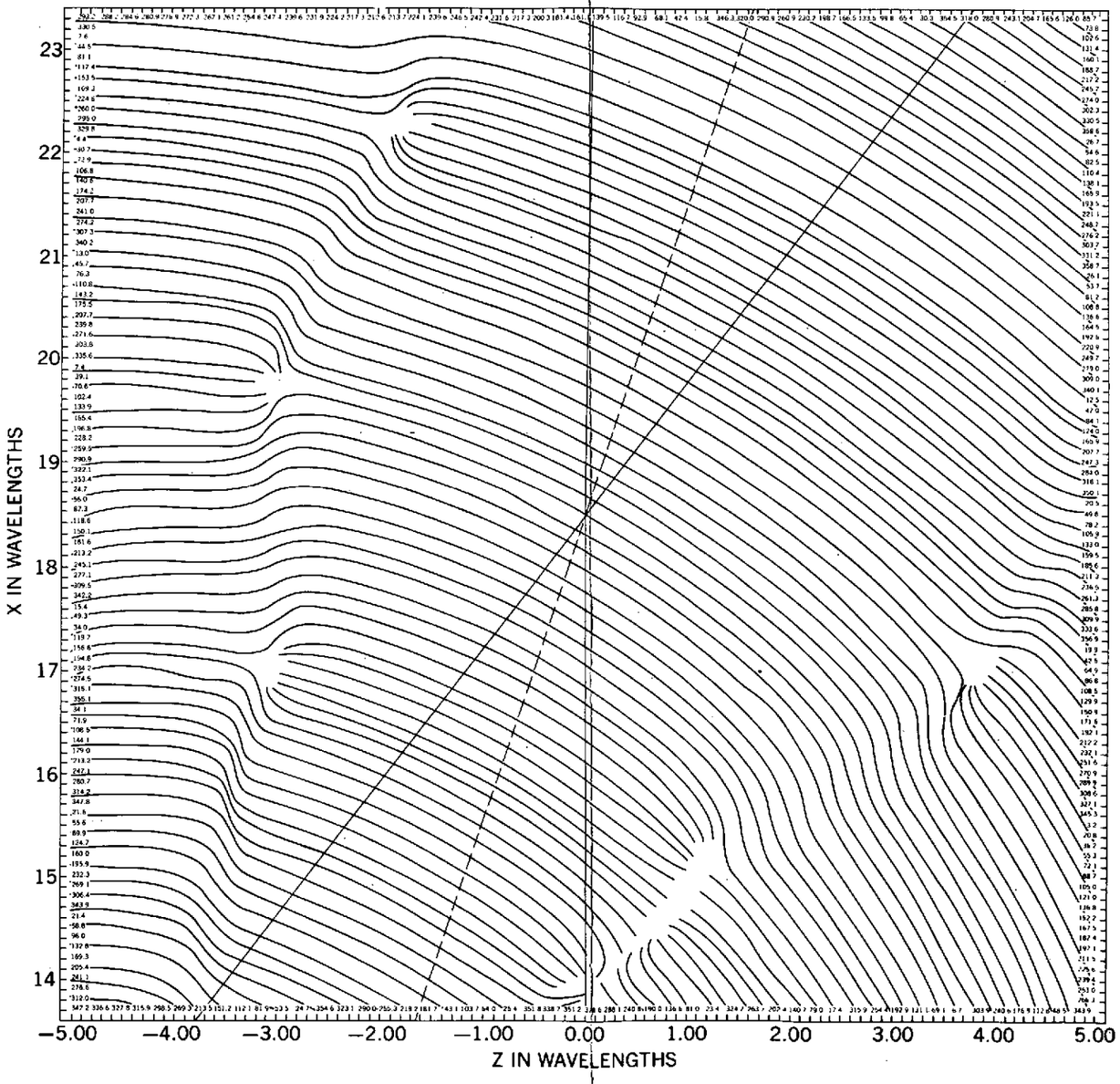

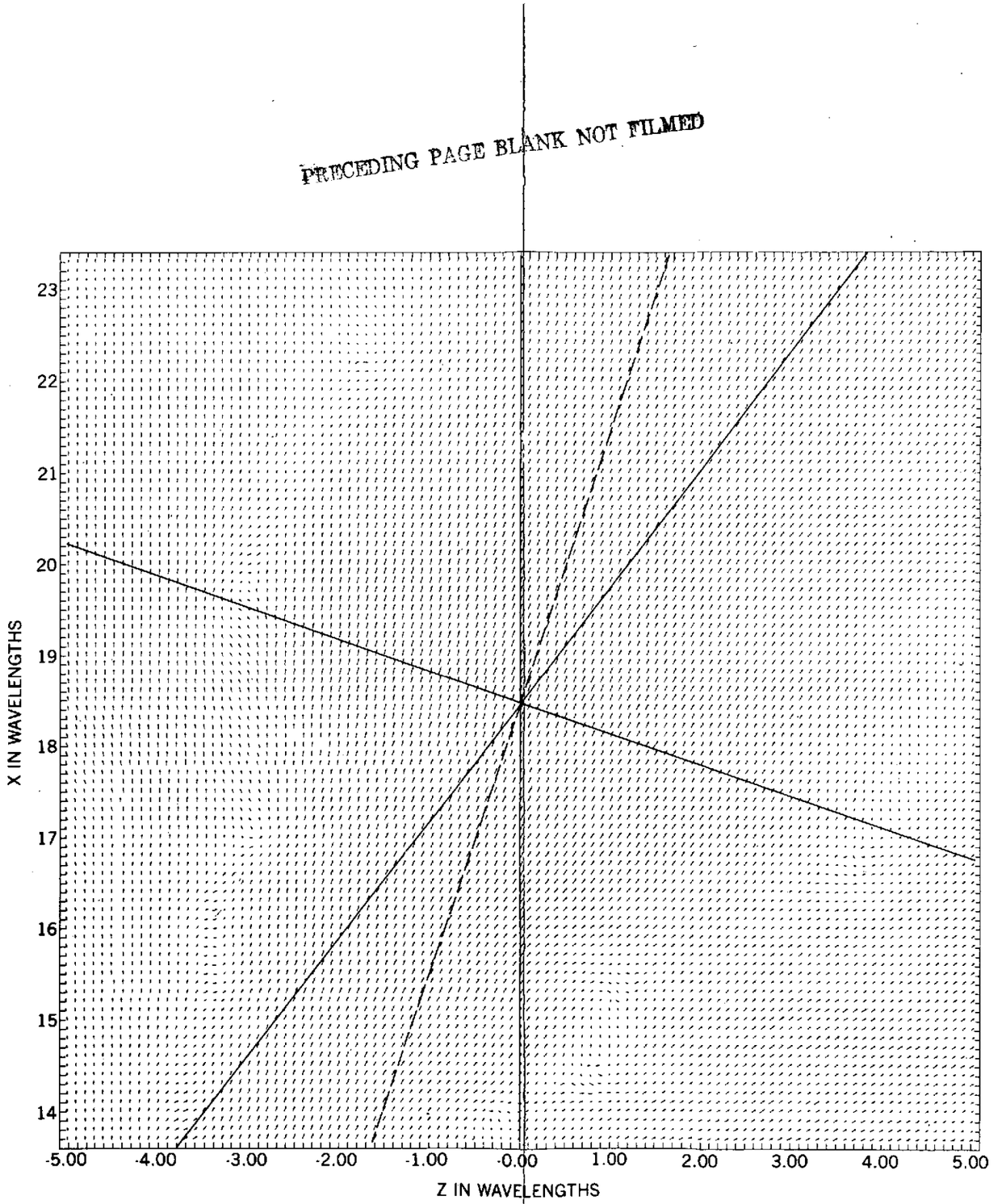

minimizes main aperture blockage due to subreflector and feed was employed. It was found that focal-region mapping and ray-tracing through the system focal point provided valuable insight for achieving bidirectional squint with a single feed.

The geometry originally intended as a candidate for the US MNBS Project was adapted to bidirectional analogue "zooming" of monopulse sum and difference patterns by utilizing a pair of feeds for each (diamond monopulse) error channel. Details of this work can be found in an invention disclosure GSC-11, 862-1 dated 19 Sept. 1973.

All diffraction work on the US MNBS Project has been terminated with the submission of this report. Diffraction program development is continuing in other areas of communications, telemetry, radiometry, acquisition, and tracking. This document is an interim report.

ACKNOWLEDGMENTS

The author acknowledges input from the classical literature, periodicals, and journal papers. In particular the author acknowledges the IRE paper by Spencer, Holt, Johanson, and Sampson concerning the arrangement of reflecting surfaces. Mr. Raymons Miezis and Mr. William Bartley of Programming Methods, Inc. provided the programming support for this task, including the plot subroutines for the near-field mappings. The author is also indebted to Mr. Anthony F. Durham, Branch Head, Antenna Systems Branch Network Engineering Division for helpful advice and discussions, to Mr. Harry Fleming for reviewing the text, and to other members of the Branch.

REFERENCES

1. Miezis, R. and Schmidt, R. F., "Radiation Pattern Calculations for an ATS-F 48-Panel Deployable-Reflector Antenna," GSFC (X-525-70-231), June 1970.

2. Lockheed Missiles and Space Company "Multibeam Antenna Study," Phase I - Final Draft, September 1972.

3. Skolnik, M. I., "Radar Handbook," McGraw-Hill Book Company, 1970.

4. Hansen, R. C., ed. "Microwave Scanning Antennas, Vol. I," Academic Press, 1964.

5. Spencer, R. C., Holt, F. S. Johanson, H. M., and Sampson, J., "Double Parabolic Cylinder Pencil-Beam Antenna," IRE Transactions-Antennas and Propagation, January 1955.

6. Wolff, E. A., "Antenna Analysis," John Wiley and Sons, Inc., 1967.

7. Schmidt, R. F., "The Calculation of Antenna Radiation Patterns by a Vector Theory using Digital Computers," GSFC (X-525-68-201), June 1968.

8. Schmidt, R. F., "The Calculation of Antenna Radiation Patterns by a Vector Theory Using Digital Computers," GSFC (X-525-68-315), August 1968.

9. Schmidt, R. F., "The Calculation of Electromagnetic Fields by the Kirchhoff-Kottler Method," GSFC (X-525-70-293), May 1970.

10. Schmidt, R. F., "The Calculation of Electromagnetic Fields in the Fresnel and Fraunhofer Regions using Numerical Integration Methods," GSFC (X-811-71-392).

11. Silver, S., ed., "Microwave Antenna Theory and Design," McGraw-Hill Book Co., Inc., 1949.

12. Schmidt, R. F., "An Analysis of Simultaneous Beam Formation by Means of Passive Scattering Matrices and Uniform Planar Antenna Arrays, GSFC (X-525-64-243), November 1964.

13. Kales, M. L., "Elliptically Polarized Waves and Antennas," Proceedings of the IRE, Vol. 39, Number 5, May 1951.

14. Beckmann, P., "The Depolarization of Electromagnetic Waves," The Golem Press, 1968.

15. Paris, D. T., and Hurd, F. K., "Basic Electromagnetic Theory," McGraw-Hill Book Company, 1969.

APPENDIX A

DUAL PARABOLIC CYLINDER GEOMETRY

A parametric representation for the surface of a parabolic cylinder is

$$x = \sigma, \quad y = \text{any value}, \quad z = \frac{\sigma^2}{4F_{c_1}} + z_1 = \frac{x^2}{4F_{c_1}} - F_{c_1},$$

and the expression for the normals to the surface can be written as

$$\bar{n} = \frac{-x\hat{i} + 2F_{c_1}\hat{k}}{(x^2 + 4F_{c_1}^2)^{1/2}}$$

These expressions and others, such as differential area, can be found in Reference 1, together with their derivations.

It is a relatively straight-forward matter to verify that a spherical wave from a point source can be converted into a virtual cylindrical wave when it is used to illuminate a parabolic cylinder from the focal axis. More precisely, a sector of the spherical wave is transformed into a sector of a cylindrical wave under ray optics. The axis of the virtual cylindrical wave will lie a focal length away from the vertex-line of the parabolic cylinder and will be orthogonal to it. The preceding is a high-frequency idealization which is more or less perfectly realized for surfaces of finite dimension and non-zero wavelength under diffraction analyses.

Two simple vector products are sufficient to establish the preceding characteristics for the virtual cylindrical wave, and these constitute a very useful device for tracing rays through reflecting optical or microwave systems. Initially let $\bar{\rho}_1$ and $\bar{\rho}_2$ be arbitrary incident and reflected vectors of equal length in the expressions governing the reflection:

$$\bar{n} \cdot (\bar{\rho}_1 + \bar{\rho}_2) = 0$$

$$\bar{n} \times \bar{\rho}_1 = \bar{n} \times \bar{\rho}_2$$

The above state that $\theta_i = \theta_r$ and $\Pi_i = \Pi_r$ for angles and planes. In particular let $\bar{\rho}_1$ be the vector from the spherical point source to the surface γ_1 at a generic point so that

$$\bar{\rho}_1 = x\hat{i} + y\hat{j} + x\hat{k} = \rho_{1x}\hat{i} + \rho_{1y}\hat{j} + \rho_{1z}\hat{k}.$$

Four equations result from the vector dot and cross products.

$$n_x(\rho_{1x} + \rho_{2x}) + n_y(\rho_{1y} + \rho_{2y}) + n_z(\rho_{1z} + \rho_{2z}) = 0 \qquad \text{(a)}$$

$$n_y(\rho_{1z} - \rho_{2z}) = n_z(\rho_{1y} - \rho_{2y}) \qquad \text{(b)}$$

$$n_z(\rho_{1x} - \rho_{2x}) = n_x(\rho_{1z} - \rho_{2z}) \qquad \text{(c)}$$

$$n_x(\rho_{1y} - \rho_{2y}) = n_y(\rho_{1x} - \rho_{2x}) \qquad \text{(d)}$$

Equations (b) and (d) both lead to the same conclusion that

$$\boxed{\rho_{2y} = \rho_{1y} = y}$$

when the expression for the normal is utilized. Equations (a) and (c) can be combined with the parametric representation of the parabolic cylinder to force the conclusion that

$$\boxed{\rho_{2x} \equiv 0}$$

The latter fact can be applied to equation (a), which then yields

$$\boxed{\rho_{2z} = \frac{x^2}{2F_c} - z}$$

so that the components (ρ_{2x} , ρ_{2y} , ρ_{2z}) of the reflected ray are now available for the analysis. Figure A-1 shows the incident ray ($\bar{\rho}_1$), the reflected ray ($\bar{\rho}_2$), the parabolic cylinder, and the apparent axis of the virtual cylindrical wave.

The location of the axis of the virtual cylindrical wave is easily determined using a similar triangle relationship.

$$\frac{\rho_{2y}}{\rho_{2z}} = \frac{2\rho_{2y}}{L}$$

But the distance from FA_1 to the tip of $\bar{\rho}_2$, along z, is

$$\Delta L = \rho_{2z} \oplus z$$

where $\oplus$ is indicated since r_{2z} and z are signed. Then the distance D from FA_1 to FA_1', along z, is

$$D = L - \Delta L = 2F_{c1}$$

This shows that the axis of the presumed virtual cylindrical wave lies a distance F_{c_1} away from the vertex line of the parabolic cylinder, and is orthogonal to it.

It remains to demonstrate that the rays which appear to emanate from FA_1' actually form a cylindrical set of wavefronts. If such a wave exists, the total optical path length is the sum of $|\bar{\rho}_1|$ and $|\bar{\rho}_2|$, and equals the radius $|\bar{R}_c|$ of such a presumed wavefront. That is

$$|\bar{\rho}_1| + |\bar{\rho}_2| = |\bar{R}_c|$$

It is noted that $|\bar{\rho}_1| = |\bar{\rho}_2|$ is not a condition here, as it was in the derivation of the components or resolutes of $\bar{\rho}_2$ previously. Referring again to Figure A-1 it can be seen that it is generally true that

$$\overline{\rho}_1 = -2F_{c_1}\hat{k} + x\hat{i} + \overline{\rho}_1'.$$

Also,

$$\overline{\rho}_1' + \overline{\rho}_2 = \overline{R}_c$$

where $\overline{\rho}_1'$ and $\overline{\rho}_2$ are colinear. It follows that

$$\boxed{|\overline{\rho}_1'| + |\overline{\rho}_2| = |\overline{R}_c| = |\overline{\rho}_1| + |\overline{\rho}_2|}$$

if the wavefronts of a virtual cylindrical wave exist. Therefore only

$$|\overline{\rho}_1'| = |\overline{\rho}_1|$$

needs to be established, which is reminiscent of the virtual path-length viewpoint associated with Cassegrain, Gregorian and other systems.

Now the conclusion is immediate since

$$|\overline{\rho}_1 + 2F_c\hat{k} - x\hat{i}| = |\overline{\rho}_1|$$

reduces to

$$|y\hat{i} + (z + 2F_c)\hat{k}| = |x\hat{i} + y\hat{j} + z\hat{k}|$$

That is, the length of $\overline{\rho}'$ and $\overline{\rho}_1$ are equal because

$$y^2 + (z + 2F_c)^2 = x^2 + y^2 + z^2$$

yields the equation of the assumed parabolic cylinder.

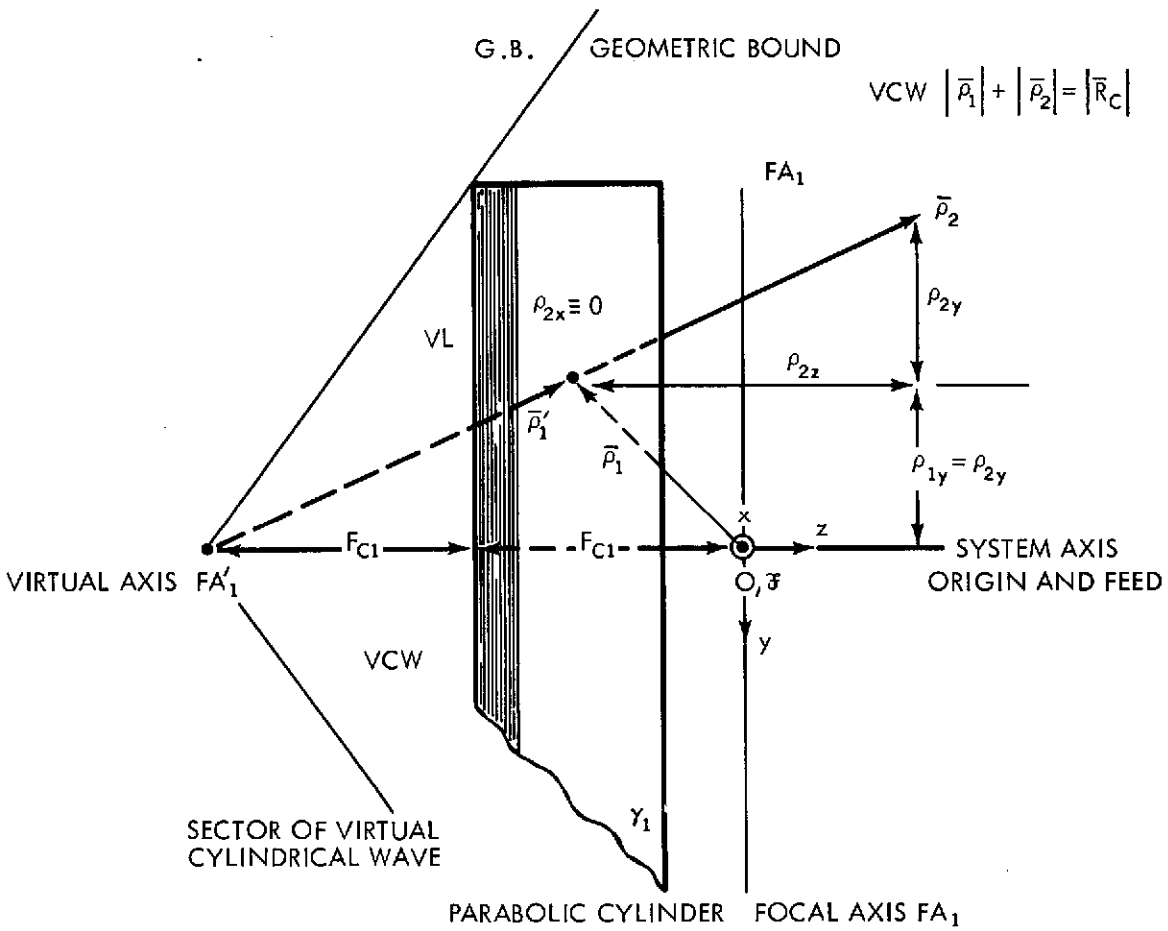

Figure A-1. Derivation of the virtual cylindrical wave.

APPENDIX B

PARABOLIC CYLINDER INTERSECTION

The "sugar scoop" geometry can, without loss of generality, be characterized by

$$z = \frac{x^2}{4F_{c_2}} - F_{c_2}$$

and

$$x = \frac{y^2}{2F_{c_1}} + F_{c_1}$$

The feed is then assumed to be situated at

$$\vec{\rho}_\epsilon = x_\epsilon \hat{i}_x = 2F_{c_1} \hat{i}_x = 2F_{c_1} \hat{i}$$

From the preceding,

$$z = \frac{\left(\frac{y^2}{4F_{c_1}} + F_{c_1}\right)^2}{4F_{c_2}} - F_{c_2}$$

The parametrization of the intersection ($\cap$) of the two parabolic cylinders is then given by:

$$x = \frac{t^2}{4F_{c_1}} + F_{c_1}$$

$$y = t$$

$$z = \frac{\left(\frac{t^2}{4F_{c_1}} + F_{c_1}\right)^2}{4F_{c_2}} - F_{c_2}$$

where the focal lengths associated with the parabolic cylinders may be qual or unequal.

APPENDIX C

THE NEAR-FIELD FORMULATION

In the transmit mode of operation the fields due to the main parabolic cylinder (γ_2) of the system are given by

$$\bar{E}(x',\ y',\ z') = \frac{1}{j\omega\epsilon}\ \frac{1}{4\pi}\int_{\gamma_2} [(\bar{n}\times\bar{H})\cdot\nabla)]\ \nabla\psi ds - j\omega\mu\ \frac{1}{4\pi}\int_{\gamma_2} (\bar{n}_2\times\bar{H}_2)\ \psi ds,$$

$$\bar{H}(x',\ y',\ z') = \frac{1}{4\pi}\int_{\gamma_2} (\bar{n}_2\times\bar{H}_2)\times\nabla\psi ds,$$

where

$$\psi = \frac{e^{-jkr}}{r}$$

and

$$\nabla\psi = -\left(jk + \frac{1}{r}\right)\psi\hat{i}_r,$$

taking $\hat{i}_r$ in a local context on the reflecting surface.

Since only the magnetic field $\bar{H}_2$ is required on γ_2, the integral

$$\bar{H}_2(x_2',\ y_2',\ z_2') = -\frac{1}{4\pi}\int_{\gamma_1} (\bar{n}_1\times\bar{H}_1)\times\nabla\psi ds$$

over the subsystem parabolic cylinder (γ_1) is sufficient to obtain the illumination of γ_2 due to γ_1.

The preceding formulation is applicable in both far-field (Fraunhofer) regions and intermediate near-field (Fresnel) regions and is particularly well-suited to dual- or multiple-reflector systems where a point on one surface may lie in the Fresnel region of another surface over which an illumination distribution is being integrated. It can be shown that the formulation used here is

identical to the Kirchhoff-Kottler and Franz formulations, but is better-suited to numerical integration methods than the latter.